JOURNAL OF MATERIALS SCIENCE 32 (1997) 4355–4376

Behaviour of 316 Ti stainless steel in deuterium oxide with chloride

G. BELLANGER
Department Tritium-137, Commissariat à l'Energie Atomique, Centre d'Etudes de Valduc, F21120 Is sur Tille, France

J. J. RAMEAU
C.R.E.M.G.P., E.N.S.E.E.G./I.N.P.G., Domaine Universitaire, B.P. 75, F38402 Saint Martin d'Hères, France

Since tritiated water contains deuterium oxide, we require a better understanding of stainless steel corrosion in tritiated water and thus we have compared the behaviour of 316 Ti stainless steel in ^2H_2O and H_2O with and without chloride. This was done by anodic polarization curves, cyclic voltammetry and electrochemical impedance spectroscopy. The corrosion potential of 316 Ti stainless steel in deuterium oxide changes and is related to pH modification due to the dissociation constant of this aqueous medium which shows the importance of pH in passivity. Without chloride, the insulating properties of the passive oxide layer depending on the pH and passive potentials are enhanced with ^2H_2O. With deuterium oxide containing chloride at near neutral pH, the repassive potential is lower than that obtained with H_2O, consequently localized corrosion in grain boundaries and pit propagation, which lead to crevice corrosion, are greater. The critical pitting potential is in transpassivity indicating that pitting is less likely to occur. Comparison with and without Cl^- for the passive potentials near the corrosion potential, shows that although chloride reduces the insulation provided by the passive oxide layer it is still greater than that obtained with H_2O.

1. Introduction

In this work, the passivity of 316 Ti stainless steel with respect to its application in tritium reprocessing installations was studied. The specific case study undertaken in this work concerns deuterium oxide. Deuterium is used in deuterated-tritiated titanium targets which are bombarded in electrostatic accelerators to produce fast neutrons and α particles of 14.1 and 3.5 MeV, respectively, by the reactions shown as Equations 1 and 2 with the formation of fluxes between 10^8–10^{13} n cm^{-2} s^{-1} for use, in hospitals and fusion studies. The quantity of tritium trapped on the target ranges between 0.04–40 TBq. Due to the production of these targets, tritiated water contains the three hydrogen isotopes.

$$^2H + {}^3H \rightarrow {}^4He + n + \alpha \quad \Sigma E = 17.6\,MeV \quad (1)$$

$$^2H + {}^2H \rightarrow {}^3He + n + \alpha \quad \Sigma E = 3.3\,MeV \quad (2)$$

Tritium decays with the emission of a β^- particle resulting in the production of radiolytic products in tritiated water. The effects of these species on the corrosion of stainless steels was recently published by our laboratories [1–6]. Quantitative analysis of tritium distribution and stress corrosion cracking in steels has been reported [7–10]. In this case, for deuterium oxide, the dissociation constant is 14.8 [11]. The pH in ^2H_2O is thus different from that in water.

We studied the effects of added chloride since chloride containing polymers may be used in pump oils or sealing joints. Tritium easily absorbs and diffuses in organic polymers by chemical bonds, e.g., $-(R-{}^3H_2)_n-$ without degassing in air, but with possible isotopic re-exchange with water. As with water, the β^- particle energy decomposes organic polymers, when these are in contact with gaseous tritium or tritiated water. If these polymers have R–Cl bonds, the decomposition reaction is:

$$R\text{–}Cl + \beta^- \rightarrow Cl^- + CO_2 + R'- \quad (3)$$

It was observed that the decomposition of sintered Ni + PTFE or PVC composites tested in our laboratories is visible after two months and the concentrated tritiated water used (e.g., 10 TBq cm^{-3}) becomes brownish during the decomposition. This tritiated water contains an appreciable concentration of Cl^-.

An acid medium was selected since relatively concentrated nitric acid solutions are produced in tritiated water reprocessing installations during the catalytic gaseous tritium oxidation cycles at 450 °C by air and finely divided palladium. This can be explained by the effect of β^- particles on nitrogen in the air used for oxidation in tritiated water; the

0022–2461

reactions are [12–15]:

$$N_2 + \beta^- \rightarrow 2N^\bullet \quad (4)$$

$$N^\bullet + 3HO_2^- \rightarrow HNO_3 + H_2O + 2O^\bullet \quad (5)$$

The HO_2^- radical is an intermediate species produced in water radiolysis. The effects of NO_3^- and HO_2^- on corrosion have been previously reported [1, 2]. In water reprocessing, the tritiated water can be concentrated by isotopic distillation, consequently, the pH is close to neutral. At the end of the tritiated water reprocessing cycle in French facilities, it is decomposed by alkaline electrolysis, using a cathodic diffusion hollow palladium finger to obtain pure gaseous tritium which is further enriched by isotopic separation in a chromatographic column. Due to these processes, we investigated alkaline, acid and near neutral pH conditions. The effects of Cl^- with deterium oxide were studied at different concentrations and in comparison to light water and with or without Cl^- for the range of the corrosion, passive and localized corrosion potentials by means of anodic polarization curves, cyclic voltammetry and electrochemical impedance spectroscopy.

2. Experimental procedures

Equivalent amounts of sodium hydroxide and sulphuric acid were added to deuterium oxide and light water (Table I). As expected, the dissociation constant difference between ^2H_2O ($pK^2_{H_2O} = 14.8$) and H_2O ($pK_{H_2O} = 14$) leads to a slight pH increase in acid media and a slight decrease in alkaline media for ^2H_2O. The chloride concentration was measured with a specific electrode.

The electrochemical equipment consisted of a Radiometer bipotentiostat and signal generator (PRT-20 and GSTP3) connected to a Tektronix 2230 numerical oscilloscope to display the currents in cyclic voltammetry. After storage in the oscilloscope, the curves were recorded on a Hewlett-Packard AXY HP 7440 plotter. The electrochemical impedance diagrams and the polarization curves obtained at a low scan rate were plotted with a Radiometer ZCP 130 T generator controlled by a Hewlett-Packard 486-25U personal computer monitored by a HP 82324 co-processor. A standard procedure was adopted in acquiring the impedance diagrams to have good data reproducibility. The spectra were obtained in potentiostatic mode where the current is free to change. The measurement sequence in passivity was: (1) to apply a given potential, E, stable to within 1 mV, first about the corrosion potential, to achieve the corresponding stationary conditions (a few min), (2) to obtain its impedance spectrum with good reproducibility, (3) to shift the potential in a positive direction up to $E + \Delta E$ and wait to ensure the new stationary condition, (4) to obtain the impedance spectrum at this new potential, and (5) to repeat the sequence from point 3 in the potential range. The frequency was scanned from high (100 kHz) to low (10 mHz) frequencies with a sinusoidal voltage variation of $\pm$ 10 mV. The Circelec computer program [16, 17] was used to interpret the experimental impedance diagrams, making it possible to obtain values of the electrical components at the electrode surface. The reference and auxiliary electrodes were, respectively, saturated calomel (SCE) and platinum electrodes. A platinum wire was connected to the reference electrode through a 0.1 μF capacitor to eliminate any possible interference and short connection leads were used to minimize inductance effects. Prior to each use in voltammetry at high or low scanning, or impedance spectroscopy, the working disk electrode was mechanically polished using 1000 mesh grade silicon carbide sheets, then with diamond paste down to 1 μm. The roughness factor, r, for polished 316 Ti steel is estimated to be in the range 1–1.6 [18–23]. The potential scanning and impedance measurements were made immediately after immersion in the electrolyte that had been deoxygenated by bubbling nitrogen for 10 min. The disk rotation speed in r.p.m. was determined in each test.

The deuterium oxide after the tests was analysed, if necessary, by atomic absorption spectroscopy (AAS-Perkin Elmer 3110) with continuum background correction (deuterium beam) and an HGA induction furnace with a pyro-coated graphite crucible equipped with a L′ Vov′ platform to enhance the measurement sensitivity. The AAS detection limit for each main alloying element – Ni, Cr, Mo, Ti and Fe – in water at a signal-to-noise ratio of 3, was about 10^{-10} mol cm^{-3}. The sensitivity (quantification limit) which characterizes the variation of the optical density value related to that of alloying element concentration, was found to be 2×10^{-10} mol cm^{-3}. The relative standard deviation of measurements obtained for several replicate determinations was about 3%. A linear calibration plot was obtained in the range from 5×10^{-10}–1×10^{-8} mol cm^{-3}. After calibration with standard solutions, four sample measurements were carried out both with and without the addition of standard solutions, to ensure the elimination of any interference between the different alloying elements. The polished 316 Ti steel surface was examined after these tests with a Cambridge S90 scanning electron microscope. The composition of the 316 Ti austenitic stainless steel, the titanium is added to improve the corrosion resistance, is given in Table II. It can be seen that there is a non-negligible carbon content.

TABLE I Dependence of pH on aqueous medium

Aliquots added (mmol)		pH	
		^2H_2O	H_2O
H_2SO_4	0.1	4.5	4
NaOH	10^{-3}	7.5	8
	20	12	12.5

TABLE II Composition of the 316 Ti steel

Elements	C	Ni	Cr	Fe	Mn	Si	Mo	Cu	Ti
(Wt %)	0.06	12	16.8	bal.	1.8	0.34	2	0.3	0.44

3. Experimental results

3.1. Results obtained with deuterium oxide or light water without chloride

3.1.1. Anodic polarization curves

Anodic polarization curves obtained for different pH values without Cl^- and at a low scan rate of $5\,mV\,s^{-1}$ are presented in Figs. 1(a and b), 2(a and b) and 3a. In these curves, the deuterium evolution potential is more negative than that of hydrogen. At alkaline and near neutral pH, the corrosion potential is shifted towards more positive values with ^2H_2O, whereas at acid pH it is shifted in the opposite direction. This is probably due to the positive and negative pH differences between ^2H_2O and H_2O (Table I). At the corrosion potential, the corrosion should occur at the cathodic and anodic sites, e.g., by the following reactions at alkaline and acid pH.

Cathodic sites:

alkaline medium: $^2H_2O + e^- \rightarrow O^2H^{\cdot} + {}^2H_{ads}$ (6)

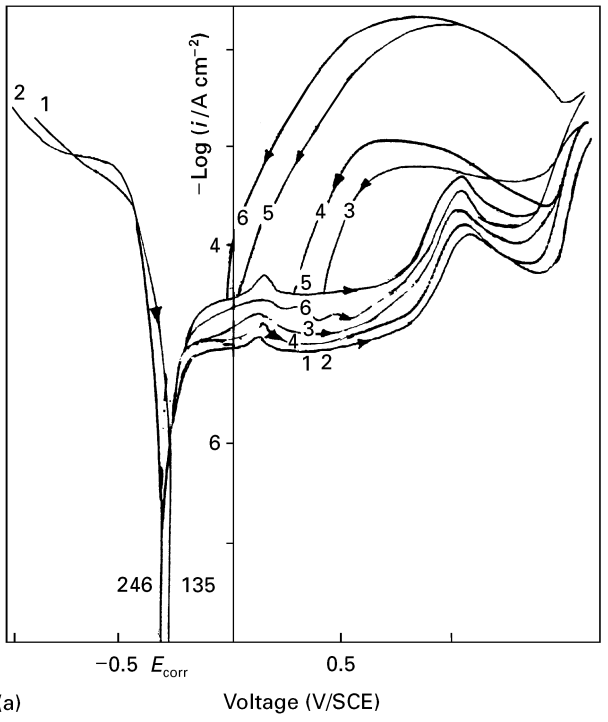

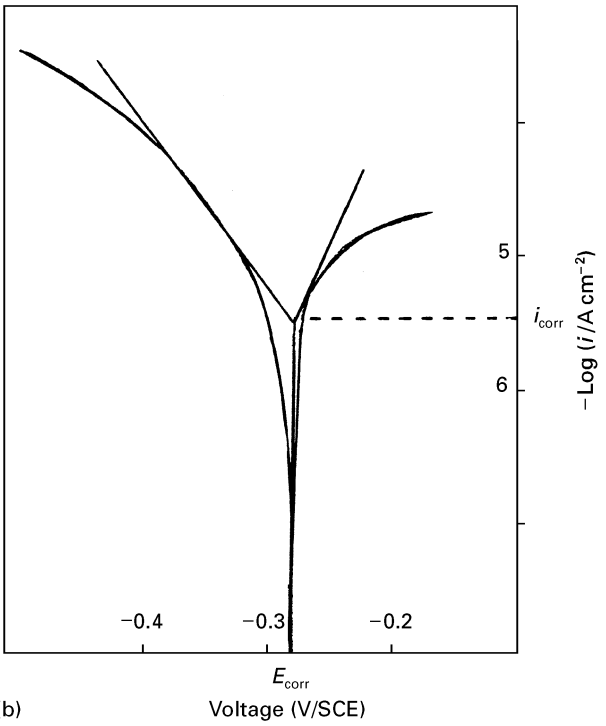

Figure 1 (a) Polarization curves with ^2H_2O or H_2O at acid pH ω: 2000 r.p.m., v: $5\,mV\,s^{-1}$, A: $0.2\,cm^2$, $0.05\,mol\,dm^{-3}$ $NaNO_3$, $\underline{H_2O}$ pH 4, $^2\underline{H_2O}$ pH 4.5, (**1**) $\underline{H_2O}$ without Cl^-, (**2**) $^2\underline{H_2O}$ without Cl^-, (**3**) $\underline{H_2O}$, $0.02\,mol\,dm^{-3}$ Cl^-, (**4**) $^2\underline{H_2O}$, $0.02\,mol\,dm^{-3}$ Cl^-, (**5**) $\underline{H_2O}$, $0.05\,mol\,dm^{-3}$ Cl^- and (**6**) $^2\underline{H_2O}$, $0.05\,mol\,dm^{-3}$ Cl^-. (b) Determination of Tafel parameters with ^2H_2O $1-\alpha = -110\,mV$, $\alpha = 50\,mV$.

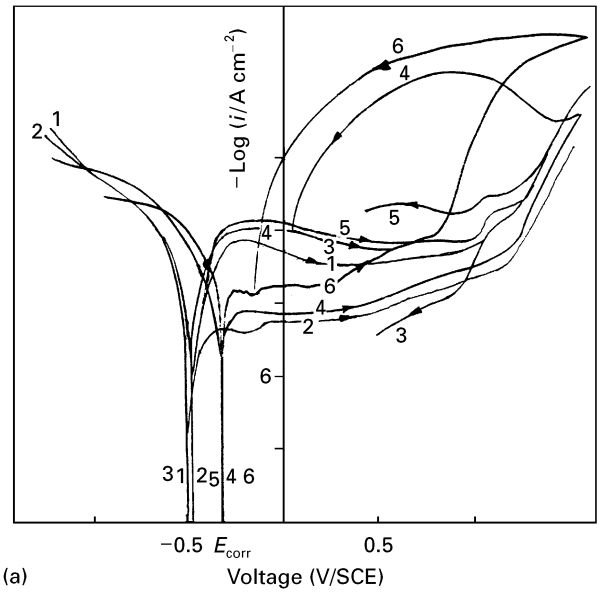

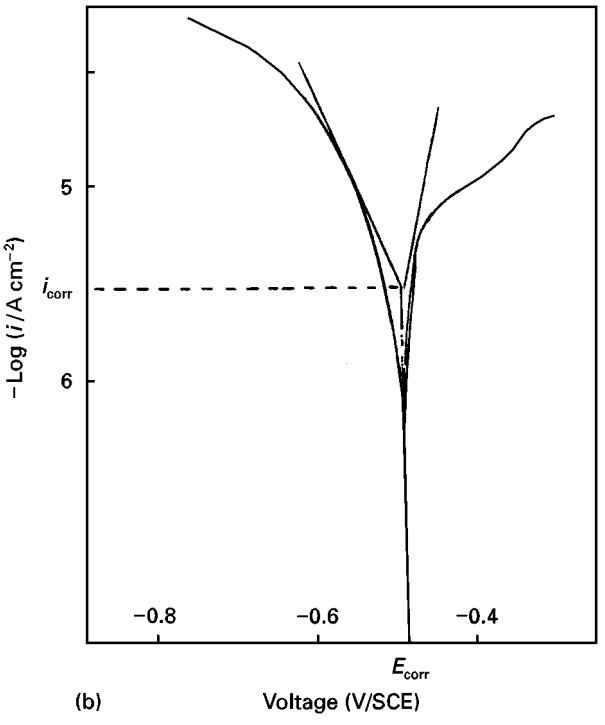

Figure 2 (a) Polarization curves with ^2H_2O or H_2O at near neutral pH ω: 2000 r.p.m., v: $5\,mV\,s^{-1}$ A: $0.2\,cm^2$, $0.05\,mol\,dm^{-3}$ $NaNO_3$, $\underline{H_2O}$ pH 8, $^2\underline{H_2O}$ pH 7.5, (**1**) $\underline{H_2O}$ without Cl^-, (**2**) $^2\underline{H_2O}$ without Cl^-, (**3**) $\underline{H_2O}$, $0.02\,mol\,dm^{-3}$ Cl^-, (**4**) $^2\underline{H_2O}$, $0.02\,mol\,dm^{-3}$ Cl^-, (**5**) $\underline{H_2O}$, $0.05\,mol\,dm^{-3}$ Cl^-, and (**6**) $^2\underline{H_2O}$, $0.05\,mol\,dm^{-3}$ Cl^-. (b) Determination of Tafel parameters with ^2H_2O $1-\alpha = -105\,mV$, $\alpha = 55\,mV$.

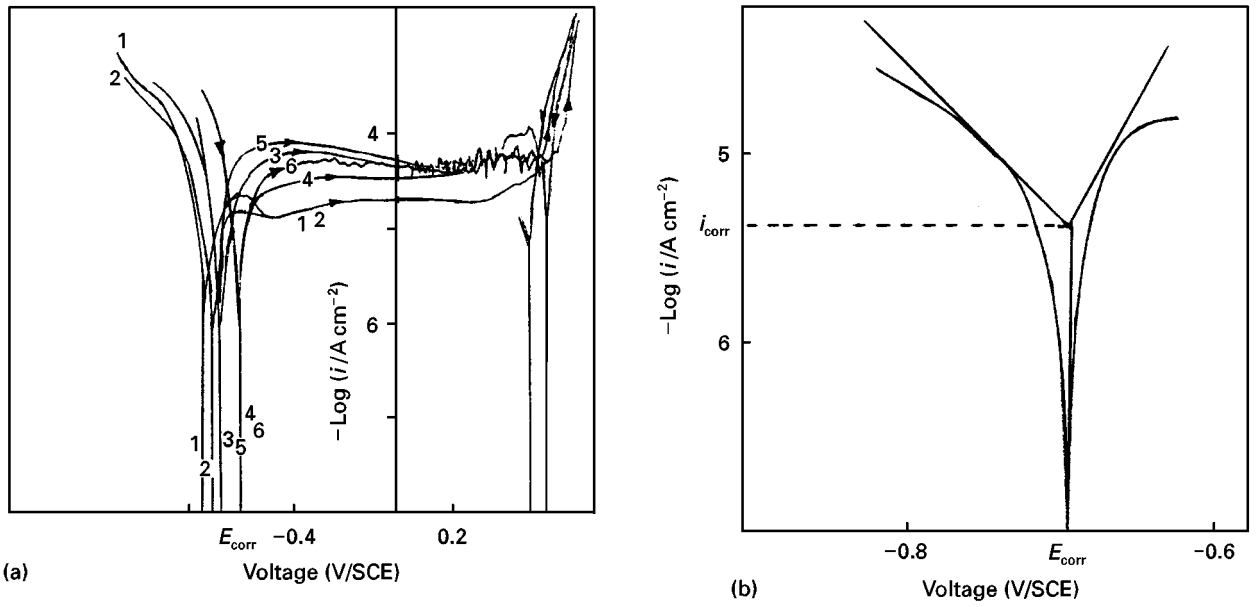

Figure 3 (a) Polarization curves with ^2H_2O or H_2O at alkaline pH ω: 2000 r.p.m., v: 5 mV s^{-1}, A: 0.2 cm^2, 0.05 mol dm^{-3} $NaNO_3$, $\underline{H_2O}$ pH 12.5, $\underline{^2H_2O}$ pH 12, (**1**) $\underline{H_2O}$ without Cl^-, (**2**) $\underline{^2H_2O}$ without Cl^-, (**3**) $\underline{H_2O}$, 0.02 mol dm^{-3} Cl^-, (**4**) $\underline{^2H_2O}$, 0.02 mol dm^{-3} Cl^-, (**5**) $\underline{H_2O}$, 0.05 mol dm^{-3} Cl^- and (**6**) $\underline{^2H_2O}$, 0.05 mol dm^{-3} Cl^-. (b) Determination of Tafel parameters with ^2H_2O $1-\alpha=-120$ mV, $\alpha=60$ mV.

TABLE III Dependence of E_{corr} and i_{corr} on H_2O or ^2H_2O for different pH

	H_2O			^2H_2O		
pH	4	8	12.5	4.5	7.5	12
E_{corr} (V/SCE)	−0.25	−0.5	−0.75	−0.28	−0.48	−0.7
i_{corr} (μA cm^{-2})	6	5	7	5	4	6

$$\text{acid medium: } {}^2H^+ + e^- \rightarrow {}^2H_{ads} \quad (7)$$

$$2\,{}^2H_{ads} \rightarrow 2\,{}^2H \quad (8)$$

The cathodic currents in the above reactions are:

$$i_c = -k_c F[{}^2H_2O]^{vred} \exp(-FE/2RT) \quad (9)$$

$$i_c = -k_c F[{}^2H^+] \exp(-FE/2RT) \quad (10)$$

anodic sites:

$$Me + 2O^2H^- \rightarrow Me(O^2H)_{2ads} + 2e^- \quad (11)$$

$$Me(O^2H)_{2ads} + O^2H^- \rightarrow MeOO^2H + {}^2H_2O \quad (12)$$

$$i_a = 2k_a F[O^2H^-]^{vox} \exp(FE/RT) \quad (13)$$

where the different k are the anodic and cathodic reaction rate constants and v the electrochemical reaction orders, and $MeOO^2H$ is the "wet" oxide together with "dry" Me_2O_3 formed on 316 Ti steel. In Equation 13, F is the Faraday constant, E the applied potential, T the temperature and R is a constant. The size and characteristics of the oxide layer change with the potential and with other factors such as the aqueous medium. In these curves, the passive currents are lower for pH 7.5 and with ^2H_2O. The explanation for the lower currents could be that deuterium oxide leads to less dissociated "wet" deuterated metal oxide and more insulating "dry" oxide. These equations show that O^2H^- are consumed in anodic sites and produced in cathodic sites resulting in local pH modifications as demonstrated by previous work in our laboratories [24].

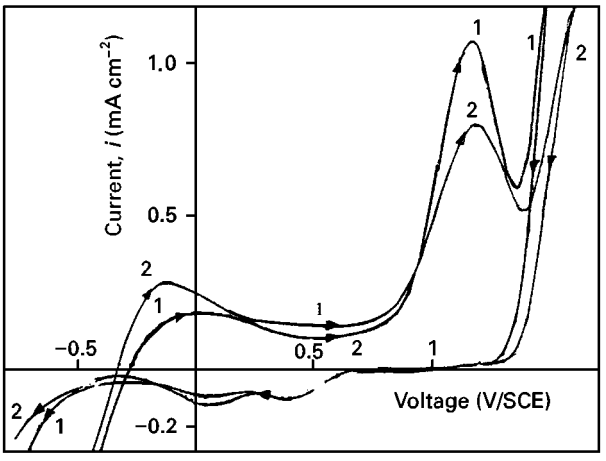

Figure 4 Voltammetric curves with ^2H_2O or H_2O at acid pH ω: 2000 r.p.m., v: 100 mV s^{-1}, A: 0.2 cm^2, 0.05 mol dm^{-3} $NaNO_3$, without Cl^-, (**1**) $\underline{H_2O}$ pH 4 and (**2**) $\underline{^2H_2O}$ pH 4.5.

Equations 11 and 12 contribute to the passivity by means of $Me(O^2H)_{2ads}$ and Me_2O_3. The corrosion potential of this system is the potential at which both the cathodic and anodic currents are equal. From these equations, $E_{corr.}$ is assumed to be:

$$E_{corr.} = \frac{1.15\,RT}{F}\left(\log\frac{k_c}{k_a} + \nu pH\right) \quad (14)$$

According to Equation 14, plotting $E_{corr.}$ against pH should give a straight line:

$$\frac{\partial E_{corr.}}{\partial pH} = \frac{1.15\nu RT}{F} \quad (15)$$

It can be seen that the pH variation with deuterium oxide (Table I) modifies the corrosion potential as shown by the experimental values in Table III where the slope is about 57 mV per pH decade. The reaction order sign (ν) expected for ^2H_2O is consequently

negative which clearly indicates the cathodic electrochemical reaction [25]. The cathodic and anodic experimental Tafel slopes obtained from the Radiometer software program (Figs. 1(a and b), 2(a and b) and 3b) are, respectively, approximately −110 and 55 mV per decade and are consistent with Equations 9, 10 and 13.

As in Equation 14, the corrosion current is, e.g., for alkaline pH:

$$i_{\text{corr.}} = 2k_a F\left(\frac{k_c}{k_a}\right)^{0.66} (O^2H^-)^{0.3\nu} \qquad (16)$$

The corrosion current, $i_{\text{corr.}}$, depends on O^2H^- activity, therefore on pH modification by deuterium oxide. The values determined from the experimental data using the Radiometer software program are given in Table III. In this table, it can be seen that the value of $i_{\text{corr.}}$ is lower with ^2H_2O. These values show better protection with deuterium oxide.

In the transpassivity, it is observed that the anodic current increases with ^2H_2O or H_2O signifying corrosion of 316 Ti steel.

3.1.2. Voltammetric curves

The use of relatively fast scan rates is unusual in corrosion testing, and the justification for this technique is given by Morris and Scarberry [26]. With the rapid-scan curves, it is easier to find peaks and inflections where the slow-scan curves suggest they might exist. Figs. 4, 5 and 6 illustrate the voltammograms obtained with deuterium oxide and light water and a scan rate of 100 mV s^{-1}. Evidently the presence of ^2H_2O significantly affects the 316 Ti steel oxidation and reduction processes. On increasing the potential in the forward scan, a prepassive peak is seen at alkaline pH. At more acid pH, the prepassive peak is hidden to a greater extent by the deuterium and hydrogen evolution current. The size of the prepassive peak changes or disappears depending on whether or not there is deuterium oxide (Fig. 5). In the backward scan, a major reduction peak occurs near − 0.8 V/SCE as seen at alkaline or more neutral pH and corresponds to the reduction of corrosion products. Near neutrality and with ^2H_2O, the passive current is fairly low and shows that the oxide layer is an excellent isolating barrier. It should be noted that the passive region is followed by a transpassive peak preceding the oxide layer dissolution and oxygen evolution potentials. The current increases quickly in this region. The reaction concerning the

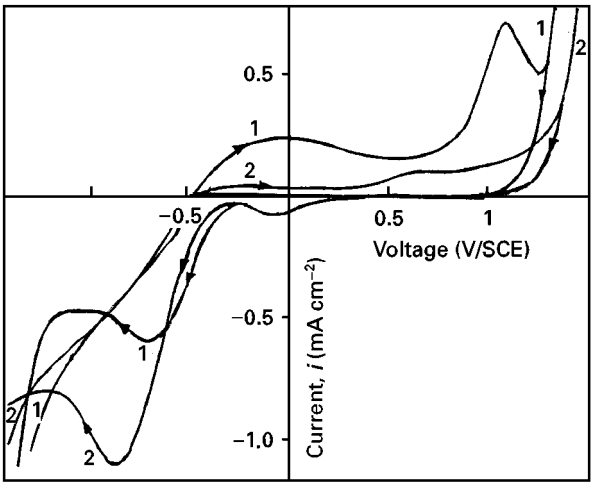

Figure 5 Voltammetric curves with ^2H_2O or H_2O at near neutral pH ω: 2000 r.p.m., v: 100 mV s^{-1}, A: 0.2 cm^2, 0.05 mol dm^{-3}, $NaNO_3$, without Cl^-, (**1**) $\underline{H_2O}$ pH 8 and (**2**) $^2\underline{H_2O}$ pH 7.5.

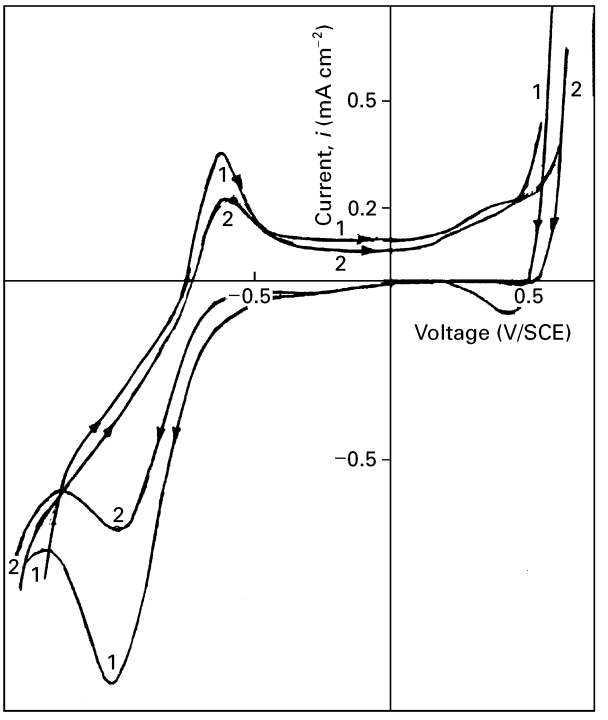

Figure 6 Voltammetric curves with ^2H_2O or H_2O at alkaline pH ω: 2000 r.p.m., v: 100 mV s^{-1}, A: 0.2 cm^2, 0.05 mol dm^{-3}, $NaNO_3$, without Cl^-, (**1**) $\underline{H_2O}$ pH 12.5 and (**2**) $^2\underline{H_2O}$ pH 12.

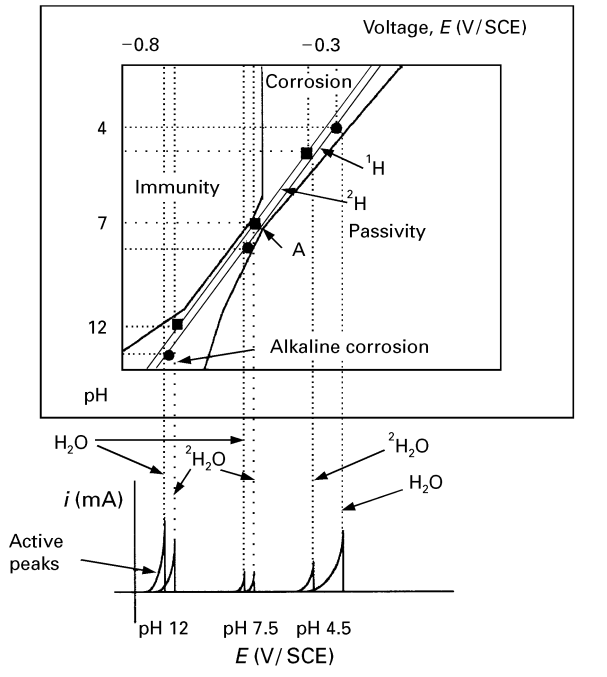

Figure 7 Diagram giving the behaviour of 316 Ti steel in chloride-free solution (top), polarization curves at pH 4–12 (bottom), experimental circumstances of general corrosion, alkaline corrosion and passivity [27].

transpassive region is:

$$MeOO^2H + 2\,{}^2H_2O \rightarrow MeO_4^{2-} + 5\,{}^2H^+ + 3e^- \quad (17)$$

In this equation, it is clear that the passive oxide participates in the production of MeO_4^{2-}. Evidently, the presence of ^2H_2O significantly affects the oxidation and reduction processes of 316 Ti steel as with H_2O and leads to a local acidification whose effect on corrosion is inhibited by stirring [24]. Due to less alkaline and acid pH with ^2H_2O, the transpassive peak is smaller with this medium.

Moreover, the curves exhibit the following characteristics: (a) in the forward scan, the anodic curves intersect the potential axis at more positive potentials with ^2H_2O and for alkaline and near neutral pH, (b) a lower reduction peak is obtained with ^2H_2O for these pH, (c) in the forward scan, the 316 Ti steel active peak disappears with ^2H_2O at close to neutral pH, (d) in the passive region, the anodic current decreases more with ^2H_2O. It would appear that the passive oxide layer is more protective with ^2H_2O, (e) in the transpassive region, the anodic peak is lower with ^2H_2O. An interpretation of this behaviour could be that the oxide breakdown current decreases. As a result, voltammograms and polarization curves show that there is modification of the passive oxide layer between ^2H_2O and H_2O.

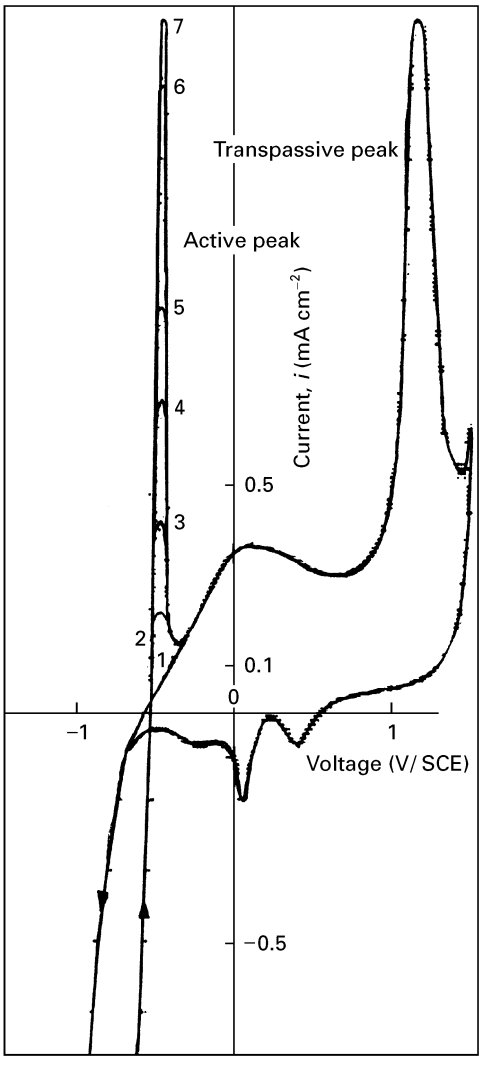

Figure 8 Active peak partially hidden by the reduction current of deuterium oxide acid pH and simulation with 3×10^{-2} mol dm^{-3} corrosion products for 316 Ti, v: 200 mV s^{-1}, $\underline{\omega}$: (1) 0, (2) 360, (3) 460, (4) 560, (5) 660 and (6) 960 r.p.m.

The tracing of voltammograms at different pH values reveals the active behaviour modifications. At the corrosion potential and the active region, the net current is equal to the sum of two currents with opposite signs: that due to 316 Ti steel oxidation and that due to ^2H_2O reduction. The explanation of active behaviour modifications is aided by reference to the diagrams in Fig. 7 which show several characteristic changes depending on pH in the Pourbaix relationship [27]:

(1) At pH 12.5 obtained with H_2O, a larger alkaline corrosion region with the formation of $HMeO_2^-$ is seen. 316 Ti steel is easily corroded with the formation of a high active peak. Higher potentials than that of alkaline corrosion correspond to the passive region. At pH 12 obtained with ^2H_2O, a narrower alkaline corrosion region is seen with the formation of passive oxide corresponding to Me_2O_3 and Me_3O_4. 316 Ti steel is passivated with the formation of a smaller active peak.

(2) At pH 7.5 obtained with ^2H_2O, the corrosion potential is more easily placed in passivity (contraction point A) than at pH 8 obtained with H_2O, therefore 316 Ti steel is passivated without the formation of an active peak. For this pH, the corrosion current should be lower than that obtained at pH 8.

(3) At pH 4 and 4.5, a wider corrosion region preceding the passivity is seen, with the possible formation of Me^{2+} and Me^{3+}. 316 Ti steel is corroded with the formation of an active peak. This peak can be partially hidden by the deuterium oxide reduction current (Fig. 8) at more acid pH. In this figure, the active peak depends on ionic species coming from the corrosion of steel in deuterium oxide whereas the transpassive peak does not depend on ionic species.

It is also necessary to compare the straight lines for deuterium and hydrogen evolution. That of deuterium is below that of hydrogen, but due to the positive and negative pH differences between ^2H_2O and H_2O (Table I), at alkaline and near neutral pH, the corrosion potential of ^2H_2O should be higher than that of H_2O, and at acid pH the corrosion potential of ^2H_2O is lower than that of H_2O. From the Pourbaix diagram, it can be seen that:

(1) At alkaline pH, the corrosion potential will be nearer potentials of the narrow corrosion region for ^2H_2O, while with H_2O, the corrosion potential will be positioned more centrally in the alkaline corrosion region resulting in a higher active peak.

(2) Near neutrality, H_2O is slightly more dissociated and the pH is 8, whereas the pH of ^2H_2O is 7.5. According to the Pourbaix relationship, at pH 7.5, the straight line for deuterium is nearer the contraction in point A. This results in more passivity than at pH 8 and a very small passive current without an active transition (Fig. 5) and higher corrosion potential as also seen in the voltammograms. Fewer corrosion

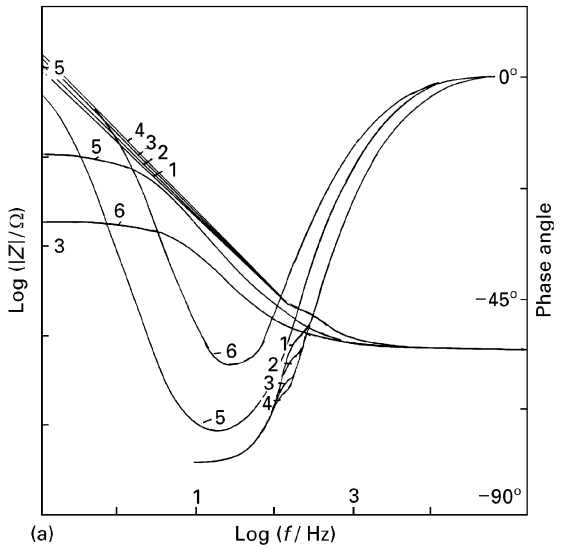

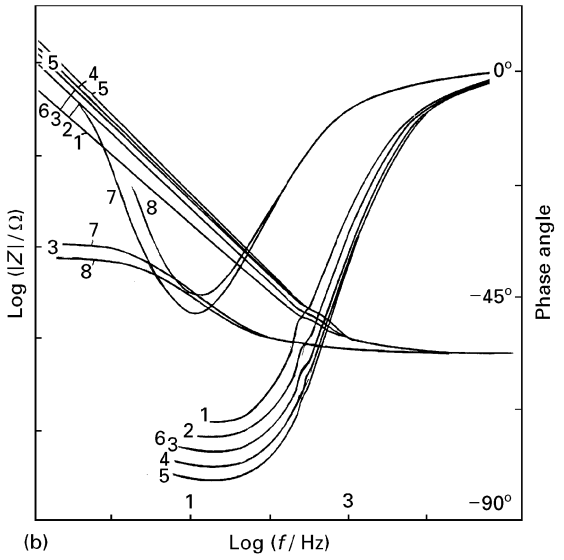

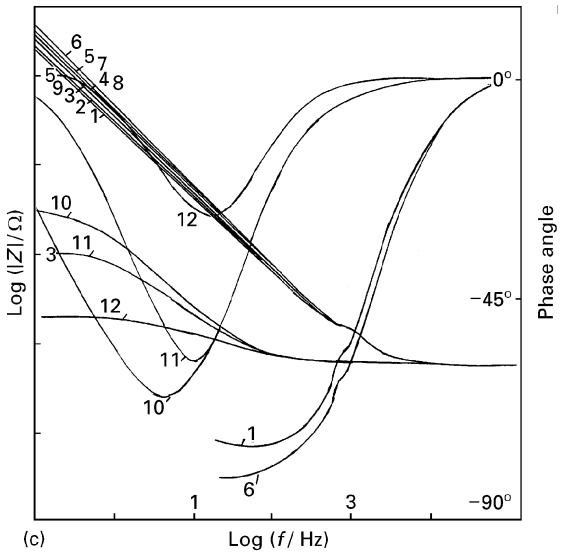

Figure 9 Experimental Bode spectra with H_2O ω: 2000 r.p.m., *A*: 0.2 cm^2, 0.05 mol dm^{-3} $NaNO_3$ (**a**) pH 4, (1) − 0.2. (2) − 0.17. (3) − 0.15. (4) − 0.12. (5) 1.375 and (6) 1.425 V/SCE (**b**) pH 8, (1) − 0.22. (2) − 0.2. (3) − 0.17. (4) − 0.15. (5) − 0.12. (6) − 0.1. (7) 1.3 and (8) 1.325 V/SCE (**c**) pH 12.5, (1) − 0.35. (2) − 0.32. (3) − 0.3. (4) − 0.27. (5) − 0.25. (6) − 0.22. (7) − 0.2. (8) − 0.17. (9) − 0.15. (10) 0.58. (11) 0.6 and (12) 0.65 V/SCE parameter values in Table IV.

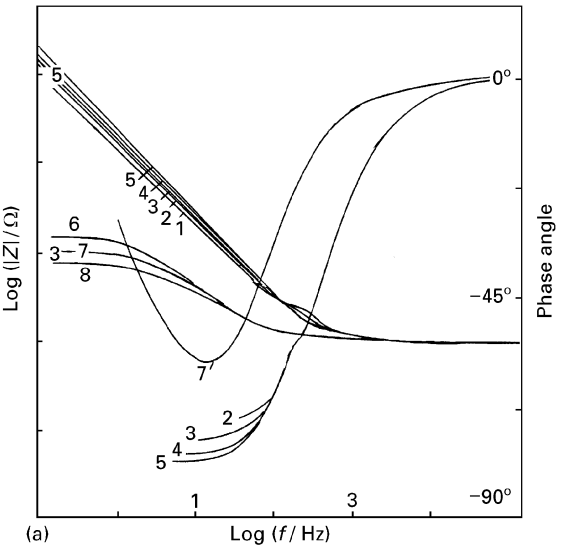

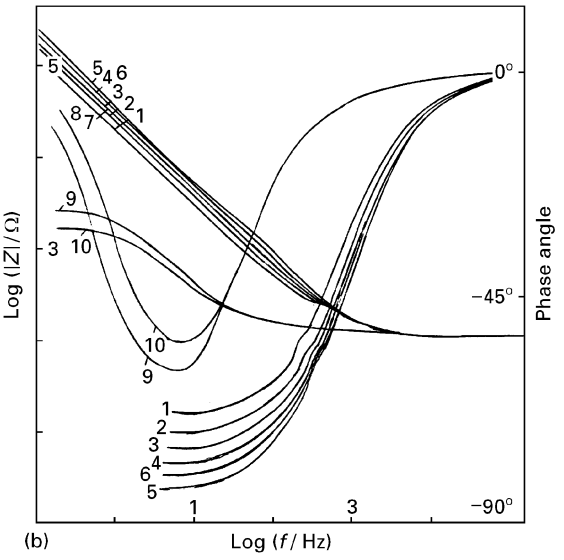

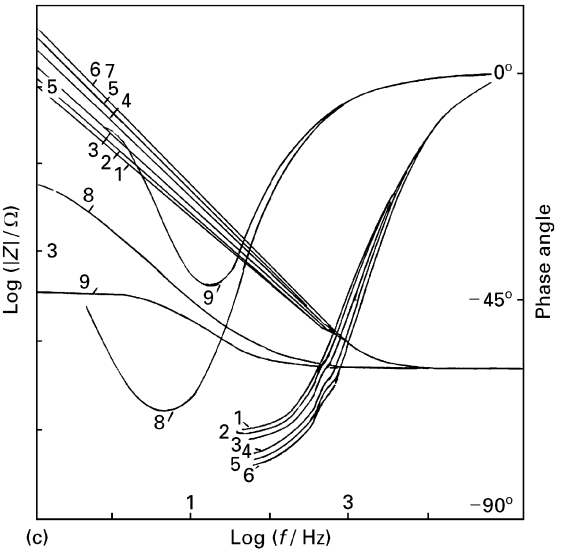

Figure 10 Experimental Bode spectra with ^2H_2O ω: 2000 r.p.m., *A*: 0.2 cm^2, 0.05 mol dm^{-3} $NaNO_3$ (**a**) pH 4.5, (1) − 0.2. (2) − 0.17. (3) − 0.15. (4) − 0.12. (5) − 0.1 (6) 1.425. (7) 1.3 and (8) 1.325 V/SCE (**b**) pH 7.5, (1) − 0.22. (2) − 0.2. (3) − 0.17. (4) − 0.15. (5) − 0.12. (6) − 0.1. (7) − 0.07. (8) − 0.05. (9) 1.3 and (10) 1.325 V/SCE (**c**) pH 12, (1) − 0.37. (2) − 0.35. (3) − 0.32. (4) − 0.3. (5) − 0.27. (6) − 0.25. (7) − 0.22. (8) 0.6 and (9) 0.65 V/SCE, parameter values in Table V.

species are formed since the reduction peak is lower than that obtained at pH 8.
(3) At acid pH, the corrosion potential of ^2H_2O is lower than that of H_2O in the voltammograms, which corresponds to the situation given in the Pourbaix relationship for pH 4.5 and pH 4. In this case the corrosion potential of ^2H_2O will be towards the contraction point whereas that of H_2O will be nearer the corrosion region. The active peak can be hidden by the cathodic current corresponding to hydrogen or deuterium evolution.

3.1.3. Impedance spectra

3.1.3.1. Results. This section is concerned with the analysis of impedance data for 316 Ti steel passivated at different passive potentials and with ^2H_2O or H_2O. The impedance data will be compared to evaluate the effect of ^2H_2O on the passive oxide characteristics. In the passive domain, the semicircles in the Nyquist plots are too incomplete over all the frequency range to be easily interpreted, therefore the Bode plots were plotted for 316 Ti steel. Comparative measurements (Figs. 9(a–c) and 10(a–c)) made at different pH, with ^2H_2O or H_2O and passive potentials near the corrosion potential (up to $+200$ mV) show changes in $\log|Z|$ and phase angle/$\log(f)$. In these figures, f is the frequency and $|Z|$ the electrode impedance. The Bode plots are essentially characterized by three distinct regions:
(a) In the higher frequency region (1–100 kHz), the Bode plot exhibits a constant (horizontal line) $\log|Z|$ versus $\log(f)$ with phase angle values near 0°. This is the response of the electrolyte resistance R_{el} (resistive region).
(b) In the broad low and middle frequency range, the diagrams display a linear slope of about -1 in $\log|Z|$ as $\log(f)$ decreases, while phase angle values approach $-90°$. This is the characteristic response of a passive oxide capacitance (C_{ox}) in the purely capacitive region. The capacitive behaviour is observed over a broad measurement frequency range.
(c) In the higher frequency range of (b), an inflection in the phase angle versus $\log(f)$ curve and the $\log|Z|$ versus $\log(f)$ plots, which can be more easily obtained by subtracting the electrolyte resistance, as shown in the simulated Bode plots (Fig. 11). These indicate the presence of a hardly identifiable parallel resistance and a non-dissipative passive oxide capacitance due to its formation. Also, the deviation of the phase angle maximum, near $-90°$, signifies that the passive layer thus formed on 316 Ti steel approaches more ideal capacitor behaviour.

According to different studies [28–30], the reciprocal space charge capacitance (C_{ox}^{-1}) is directly proportional to the oxide layer thickness. To calculate the thickness, the reciprocal capacitance value can be either taken from the Bode plot at 0.16 Hz, where the impedance data give a straight line with a slope of ≈ -1, or from the value of imaginary part of the impedance, Z_{im}, at the same frequency using the relations given by Kerrec *et al.* [31].

$$1/C_{ox} = 2\pi f Z_{im} \tag{18}$$

$$d = \varepsilon\varepsilon_0 r/C_{ox} \tag{19}$$

where d is the oxide layer thickness, r the roughness factor, ε the relative dielectric constant of the oxide, ε_0 the permittivity of free space (8.9×10^{-14} F cm^{-1}) and C_{ox} the oxide layer capacitance. As the relative dielectric constant for 316 Ti steel was not found in the literature, we measured the current dependence as a function of time during potentiostatic oxide formation at $+0.2$ V above the corrosion potentials and with ^2H_2O or H_2O and the different pH (Fig. 12). Under these conditions, the current response may be attributed to two possible processes: passive layer formation and oxide layer dissolution. Thus, we quantitatively analysed for Fe, Ni, Cr and Ti ions which could be present in deuterium oxide by AAS; before analysis, the potential was kept for 1 h at the selected value. The detection limit by AAS is found to be 10^{-10} mol cm^{-3}, while the total amount of oxide was calculated from Fig. 6 to be 2×10^{-8} mol, assuming a surface of 1 cm^2 in the tests. The double layer

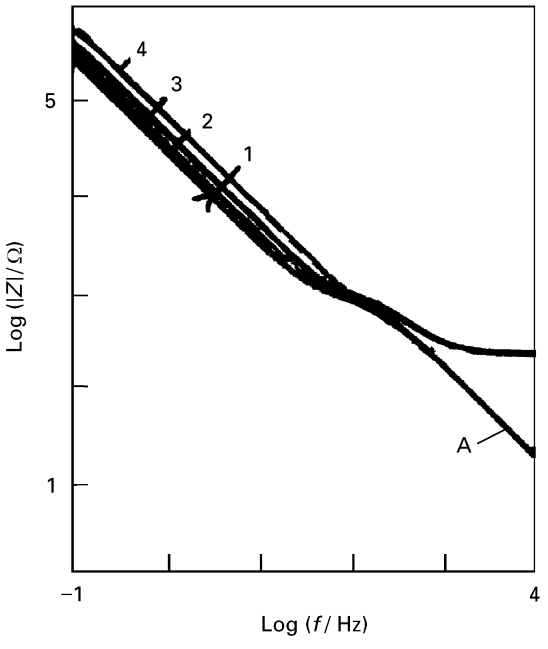

Figure 11 Simulated impedance diagrams by subtracting the electrolyte resistance (line A) according to Fig. 10a.

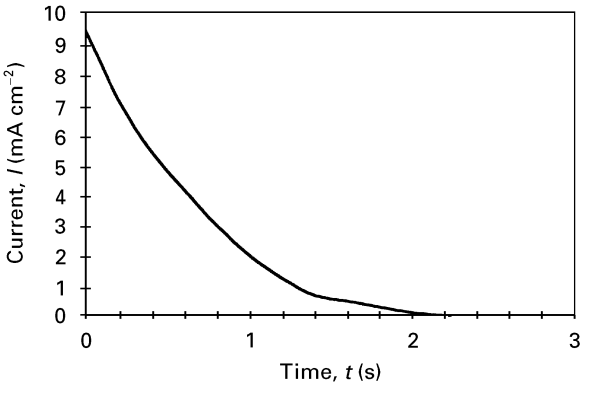

Figure 12 Current as a function of time in passivity.

charging current should be negligible (no greater than 15 μA at passive potentials). The method therefore is suitable for showing the presence of some metallic ions in deuterium oxide and determining ε. The amounts of analysed iron, nickel, chromium and titanium in the deuterium oxide were negligible. Therefore the quantity of the total charge obtained integrating the current–time curve in Fig. 12, corresponds to oxide layer formation. From Faraday's law, the oxide layer thickness, d, is calculated by another method:

$$d = QM/nF\rho r \qquad (20)$$

where Q is given in coulomb, M is the mean molar weight of the oxide, assumed to be 159, n is the mean number of electrons required to form the passive oxide and ρ the oxide density, equal to 5.2 g cm^{-3} according to Schmuki and Böhni [32]. Substitution of Equation 20 into Equation 19 therefore yields the average value of ε and gives 24. The values of passive oxide capacitance (C_{ox}) were calculated for different passive potentials and with ^2H_2O or H_2O by Equation 20 (Tables IV and V). In these tables, the variation of C_{ox} indicates that the oxide layer formation obeys a growth law depending on the passive potentials as was indicated by Schmuki and Böhni [32], pH and deuterium oxide or light water. A "critical capacitance" corresponding to its lower value denotes the perfect oxide layer. The Bode plots (Figs. 9(a–c) and 10(a–c)) allow us to calculate the flatband potential and donor or acceptor concentration (n_d) over a sufficient potential range following the simplified Mott–Schottky equation:

$$C_{ox}^{-2} = (2/\varepsilon\varepsilon_0 n_d re)(V_m - V_{fb} - kT/e) \qquad (21)$$

where e is the charge of the electron, n_d the donor density, k the Boltzmann constant, and V_m, V_{fb} the potentials at which the impedance measurements are carried out and the flatband potential, respectively. The term kT/e is 25 mV at room temperature. Assuming that additional capacitive elements such as the Helmholtz layer capacitance can be neglected, linearity is observed from about E_{corr} (Fig. 13) depending on pH and ^2H_2O or H_2. Using Equation 21, the donor-acceptor density (which corresponds to Me^{n+} metal cation in oxide) calculated from the slope is lower with ^2H_2O for the different pH (Table VI). The carrier concentration obtained with H_2O, agrees with

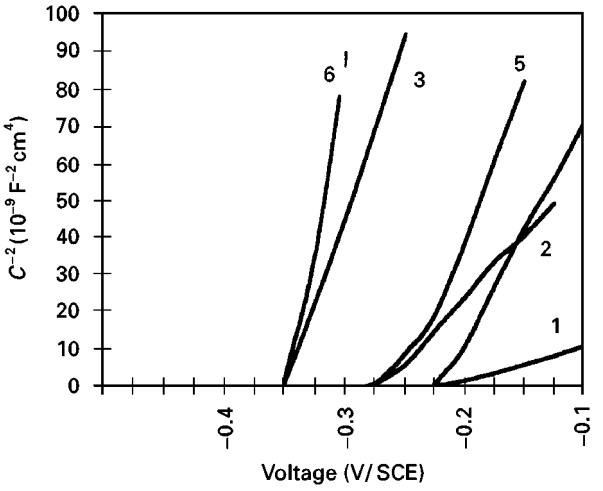

Figure 13 Mott–Schottky plots for passive oxide layer (1) H_2O, pH 4, (2) H_2O, pH 8 (3) H_2O, pH 12.5, (4) ^2H_2O, pH 4.5, (5) ^2H_2O, pH 7.5, (6) ^2H_2O, pH 12, curves 1 and 2: acid pH, curves 3 and 4: pH near the neutrality, curves 5 and 6: alkaline pH, uneven-number: ^2H_2O, even-number: H_2O.

TABLE IV Dependence of oxide capacitance (μF cm^{-2}) on passive potentials for H_2O at different pH

E/(V/SCE)	− 0.35	− 0.32	− 0.3	− 0.27	− 0.25	− 0.22	− 0.2	− 0.17	− 0.15	− 0.12
pH 4							11	10	9	6.9
pH 8						11	10	9	8.3	6.5
pH 12.5	5.3	4.8	4	3.6	3.2	2.8				

TABLE V Dependence of oxide capacitance (μF cm^{-2}) on passive potentials for ^2H_2O at different pH

E (V/SCE)	− 0.37	− 0.35	− 0.32	− 0.3	− 0.27	− 0.25	− 0.22	− 0.2	− 0.17	− 0.15	− 0.12	− 0.1
pH 4.5								8.3	7.7	6.2	5	4
pH 7.5							8.3	6.7	5.3	4.3	3.5	
pH 12	6.2	4.9	4.3	3.8	3.4	2.7	2.3					

TABLE VI Thickness and donor density dependence on H_2O and ^2H_2O

	Acid pH		pH near neutrality		Alkaline pH	
	H_2O	^2H_2O	H_2O	^2H_2O	H_2O	^2H_2O
C_{ox} (μF cm^{-2})	6.9	4	6.5	3.5	2.8	2.3
d(nm)	1.9	2.4	2.1	2.8	4.2	5.2
$n_d \times 10^{19}$	6	2	3	1	0.5	0.3

the theoretical value for a passive layer given by Castro and Vilche [33], Simoes *et al.* [34] and Rak-Hyun *et al.* [35]. The flat-band extrapolated potential depends on pH and ^2H_2O or H_2O.

The oxide layer thickness estimated from Equation 19 is thicker with ^2H_2O and alkaline pH. The donor density is lower with ^2H_2O. These values indicate less electron transfer and higher corrosion resistance. The passive oxide layer formed is more insulating for ^2H_2O and alkaline pH. These reflect the formation of a highly ordered and less defective oxide layer.

In the passive-transpassive region, the Bode plots (Figs. 9(a–c) and 10(a–c)) show a horizontal line at low frequencies (1–0.1 Hz) which corresponds to the charge transfer resistance indicating that 316 Ti steel becomes predominantly more resistive over a broad frequency range while the capacitive part is predominant only at higher frequencies. The value of the charge transfer resistance decreases when the passive potentials shift towards the transpassive region. The oxide layer thus formed on 316 Ti steel approaches less ideal capacitor behaviour and would then be less stable. These reflect the formation of a more defective oxide layer, breakdowns and oxide dissolution at these potentials.

3.1.3.2. Equivalent circuits and value determinations. Diagnostic criteria for the choice of equivalent circuits for modelling impedance data may be summarized by visual observation of the shifts in experimental Bode plots with changing passive potentials and with ^2H_2O or H_2O. It seems that at potentials in the passive region (mainly purely capacitive impedance), spectra give a perfect fit with the experimental data if the total impedance is modelled according to the equivalent circuit shown in Fig. 14a. In this circuit, the R_{el} term is the electrolytic resistance, and R_{ox} denotes the oxide formation resistance. Constant phase elements (CPE) are used instead of "ideal" capacitors to account for the slight deviations observed, such as a capacitive slope lower than -1. For a constant phase element, the impedance, Z_{CPE} is defined as [36–38]:

$$Z_{CPE} = A(j2\pi f)^{-a} \tag{22}$$

in which, a slope of $0 < a < 1$ for the experimental or simulated diagrams and a value of $j = (-1)^{1/2}$ are taken, while A is a frequency-independent constant considered as the reciprocal capacitance only if $a \approx 1$. The exponent a is related to the constant phase angle of the CPE in the complex plane: $\theta = (1 - a)\pi/2$.

One of the aims of plotting the experimental diagrams is to find the values of the main electrical elements using the Circelec software program [16, 17]. For this, in the simulated Bode plots (Fig. 11), the spectrum shapes coincide with the experimental plots (Figs. 9(a–c) and 10(a–c)) given as a function of the studied parameters. It is found that the charge transfer resistance is higher with ^2H_2O (4.4×10^2 kΩcm^2). Also, consideration of this value shows that the deuterium oxide would favour passivating.

In the passivity-transpassivity limit, the experimental diagrams obtained in Figs. 9(a–c) and 10(a–c) can be explained by the equivalent circuit shown in Fig. 14b. In this circuit, R_{ct} is the charge transfer resistance and C_{dl} reflects the double layer capacitance. The values of the charge transfer resistance obtained from the simulated spectra and Circelec software program show that the charge transfer resistance decreases (200 Ωcm^2) when the potential increases, signifying more corrosion.

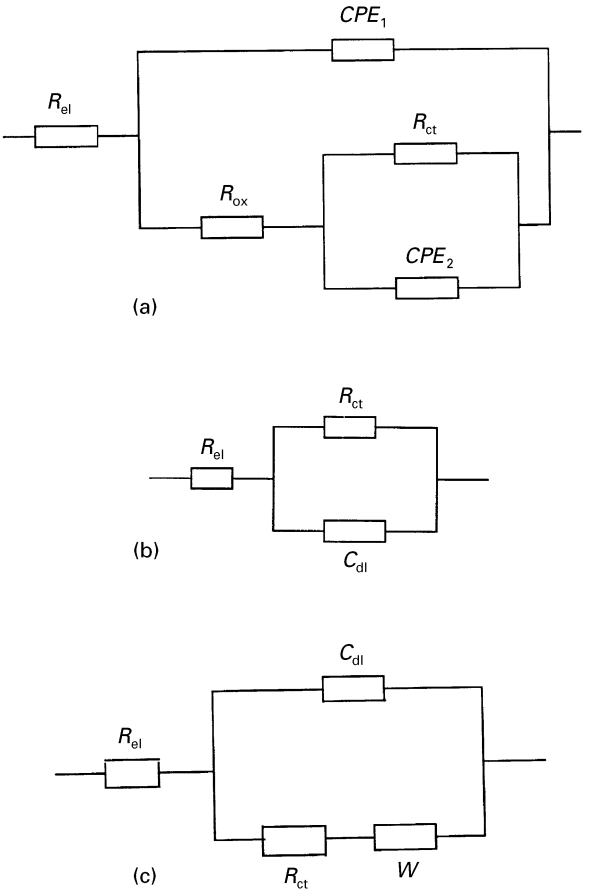

Figure 14 Equivalent circuits for impedance simulation (**a**) R_{el}: electrolyte resistance, R_{ox}: oxide resistance, CPE_1, CPE_2: constant phase elements (**b**) R_{el}: electrolyte resistance, R_{ct}: charge transfer resistance, C_{dl}: double layer capacitance (**c**) R_{el}: electrolyte resistance, R_{ct}: charge transfer resistance, C_{dl}: double layer capacitance, W: Warburg impedance.

3.1.3.3. Discussion. As indicated by Chao *et al.* [39] and Bassone *et al.* [40], it is possible to explain the presence of a diffusion controlled process within the passive oxide layer. The model has these basic features:

(a) the oxide layer contains vacancies (V_{Me}^{n+} and V_O^{2-});

(b) the vacancies are in equilibrium at $^2H_2O/H_2O$-oxide and oxide-alloy interfaces;

(c) the passive oxide layer kinetics are governed by vacancies across the oxide layer.

Based on these considerations, the following reactions, besides Equations 11 and 12, are in equilibrium at each interface:

$$\left.\begin{array}{l} Me \leftrightarrow \{oxide\} + V_{O^{2-}} \\ Me + V_{Me^{n+}} \leftrightarrow \{oxide\} \end{array}\right\} \text{alloy-oxide interface} \quad \begin{array}{l} (23) \\ (24) \end{array}$$

$$\left.\begin{array}{l} V_{O^{2-}} + {}^2H_2O \leftrightarrow 2\,{}^2H^+ + O^{2-} \\ \{\text{oxide}\} + n\,{}^2H_2O \leftrightarrow V_{Me^{n+}} + Me(O^2H)_n + n\,{}^2H^+ + ne^- \end{array}\right\} \text{oxide-deuterium oxide interface} \quad (25)\ (26)$$

where {oxide} represents metal cations in the passive oxide layer which are in equilibrium with the metal cation vacancies. Apparently, $V_{O^{2-}}$ are produced at the oxide-alloy interface and consumed at the oxide-deuterium oxide interface. As a result, $V_{O^{2-}}$ diffuses from the oxide-alloy to oxide-deuterium oxide interfaces, or equivalently, O^{2-} diffuses from the oxide-^2H_2O to oxide-alloy interfaces. Similar arguments show that $V_{Me^{n+}}$ diffuses from the oxide-deuterium oxide to alloy-oxide interfaces, and equivalently, {oxide} diffuses in the opposite direction. The net results of $V_{O^{2-}}$ migration can be seen by combining Equations 23 and 25:

$$Me + {}^2H_2O \leftrightarrow \{\text{oxide}\} + 2\,{}^2H^+ + O^{2-} \quad (27)$$

Similarly, combining Equations 24 and 26 shows that the net result of $V_{Me^{n+}}$ migration can be expressed as:

$$Me + n\,{}^2H_2O \leftrightarrow Me(O^2H)_n + n\,{}^2H^+ + ne^- \quad (28)$$

From the set of previous reactions, it is clear that the diffusion of $V_{O^{2-}}$ (or equivalently O^{2-}) results in oxide growth, depends on flatband potential, and is produced with consumption of ^2H_2O or H_2O at the oxide deuterium oxide interface, whereas the diffusion of $V_{Me^{n+}}$ (or equivalently {oxide}) is accompanied by $Me(O^2H)_n$ formation, as in Equations 11 and 12. The reactions occurring on passive oxide are influenced by the potential drops in the interfaces and within the oxide layer, $\Delta\phi$. The oxide-deuterium oxide interface is polarizable, therefore it is expected that the total potential drop is a function of deuterium oxide or light water taking into account the pH modification.

$$\partial\Delta E = \partial\Delta E_{\text{oxide–alloy}} + 2.3\alpha\frac{RT}{2F}\partial\text{pH} + \partial\Delta\phi \quad (29)$$

where α is a constant and ΔE represents the potential drop between the interfaces and within the oxide layer. It is expected that:

$$\partial(C_{ox}^{-1}) = \partial\Delta E + 2.3\alpha\frac{RT}{2F}\partial\,\text{pH} \quad (30)$$

The thickness is given by:

$$\partial d = b\left(\partial\Delta E + 2.3\alpha\frac{RT}{2F}\partial\text{pH}\right) \quad (31)$$

$$C_{V_{O^{2-}}} = \frac{M}{\rho}\exp\left[\left(\frac{\Delta G - 2F\phi}{RT}\right) + 4.6\alpha\,\text{pH}\right] \quad (32)$$

where C is the vacancy concentration with an inverse dependence on $V_{Me^{n+}}$ and $V_{O^{2-}}$, ΔG the standard Gibbs energy, b a constant resulting from considering the oxide layer as a plane capacitor. Thus Equations 29–32 represent the functional dependence of the passive layer growth law on $\partial\Delta E$ and ∂pH.

3.2. Results obtained with deuterium oxide or light water and chloride

The different experimental curves were drawn for the same previous pH, with H_2O or ^2H_2O and two Cl^- concentrations.

3.2.1. Polarization curves

According to Strehblow [41] and Chao *et al.* [39, 42], if the metal cation vacancies penetrate into the alloy at a slower rate than their diffusion through the oxide layer, they accumulate at the alloy-oxide layer interface and finally lead to a local concentration and hence will form a void. When the void grows to a certain critical size, the passive oxide layer suffers local collapse which then marks the end of the pit incubation period. The collapsed site dissolves much faster than any other location on the layer thereby leading to pit growth. From this, the diffusion of metal cation vacancies is affected by the incorporation of Cl^- ions at the oxide-^2H_2O interface as shown in the following equations.

$$\text{null} \leftrightarrow V_{Me^{n+}} + \frac{n}{2}V_{O^{2-}} \quad (33)$$

$$C_{V_{Me^{n+}}} = k(C_{V_{O^{2-}}})^{-0.5n} \quad (34)$$

$$V_{O^{2-}} + Cl^-_{\text{aqueous}} \leftrightarrow \{Cl^-\} \quad (35)$$

Equation 33 represents the Schottky-pair reaction at the oxide-^2H_2O interface. In Equation 34, $\{Cl^-\}$ is a chloride anion occupying O^{2-} vacancies. It can be seen that the number of $V_{O^{2-}}$ vacancies that are free decreases. Due to interdependence of the concentration of cation and anion vacancies and the penetration of Cl^- within the oxide layer, the number of metal cation vacancies increases in the oxide layer (Equation 34) up to a critical concentration leading to breakdown at the pitting potential. From these considerations, the criterion for pit initiation in the presence of ^2H_2O can be expressed by:

$$\frac{\partial V_{Me^{n+}}}{\partial t} = J_0[C_{V_{O^{2-}}}\{\text{oxide} - {}^2H_2O\}]^{-0.5n} \quad (36)$$

where J_0 depends on thermodynamic constants and $C_{V_{O^{2-}}}\{\text{oxide}–{}^2H_2O\}$ is the concentration of O^{2-} vacancies at the oxide layer–^2H_2O interface. Equation 36 shows that the metal cation vacancies diffusion is enhanced by decreasing the concentration of O^{2-} vacancies, e.g., with chloride present. This enhancement can effectively lead to an accumulation of metal cation vacancies at the alloy-oxide layer interface. From Equations 33 and 36, and applying a calculation procedure similar to that given by Strenblow [41] and Chao *et al.* [39, 42], we can write the simplified

equation with ^2H_2O present:

$$E_{pit} = \frac{4.6\alpha RT}{Fn}\log\left(\frac{J_m}{J_o\frac{M}{\rho}\exp\left\{\frac{pH}{RT}\right\}^{-0.5n}}\right) - \frac{2.3\alpha RT}{F}\log Cl^- \quad (37)$$

where J_m is the rate of submergence of the metal cation vacancies in the alloy. It can be seen that low submergence rates and the pH modification by ^2H_2O and H_2O change pitting by Cl^-.

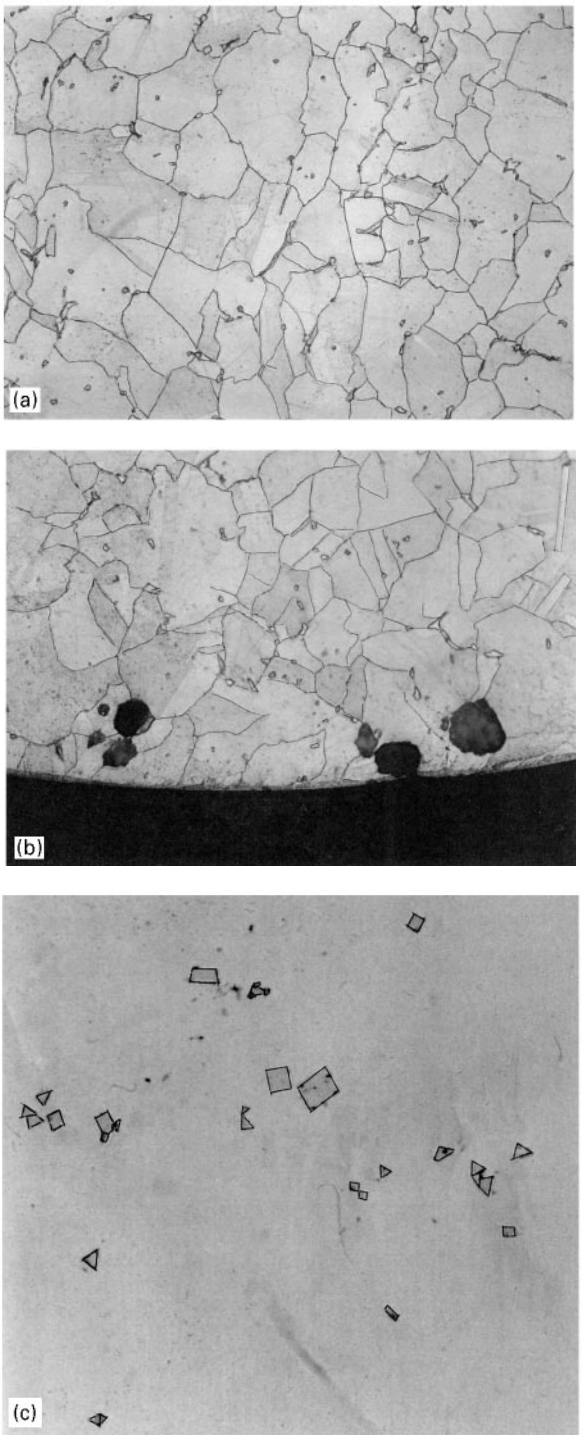

Figure 15(a–c) Metallographic examination of 316 Ti steel.

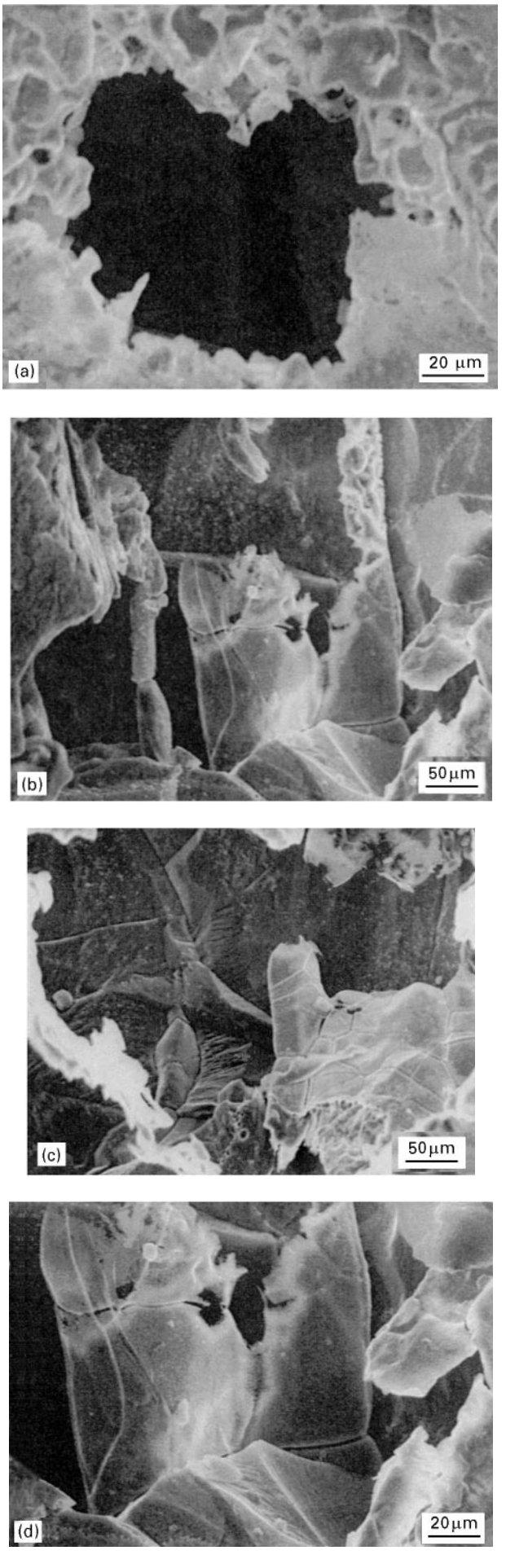

Figure 16(a–n) Scanning electron microscopy photographs of 316 Ti steel corroded in the presence of 0.02 mol dm^{-3} Cl^- in ^2H_2O at 1.5 V/SCE.

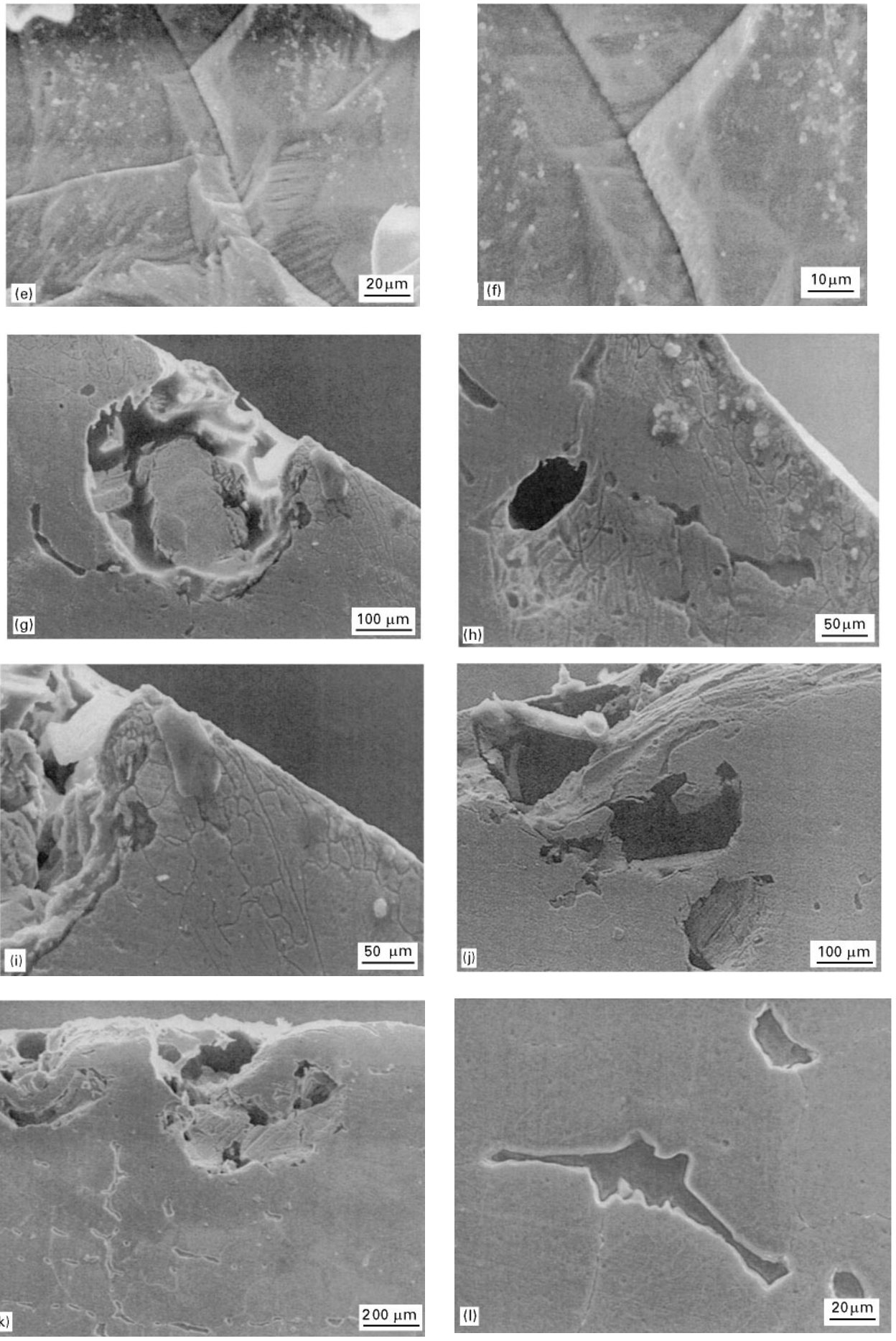

Figure 16 (Continued).

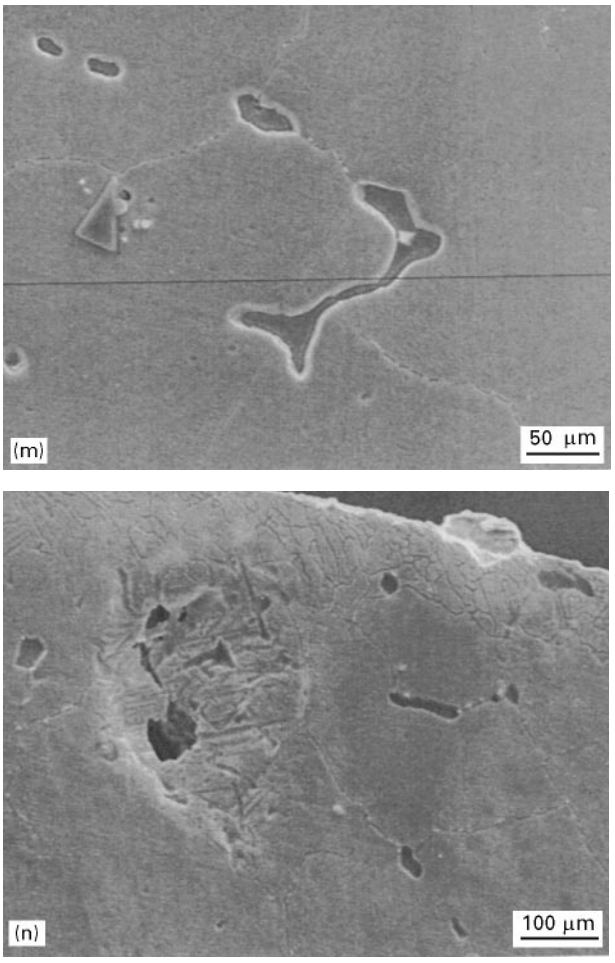

Figure 16 (Continued).

In the polarization curves, a comparison of their features allow us to determine the propensity for localized corrosion (e.g., pitting and crevice corrosion). The difference between the pitting potential and corrosion potential, and between the repassivation potential and corrosion potential, and finally the hysteresis shape are shown to be dependent on three variables used to characterize the propensity for localized corrosion. If the current in the backward scan is greater than that of the forward portion of the scan, the 316 Ti steel is predicted to be susceptible to corrosion by pitting, and if also the repassivation potentials and pitting potentials are close to the corrosion potential, the steel is predicted to be susceptible to both crevice corrosion and pitting.

In the first measurements, the effects of chloride at acid pH on pitting potentials, are observed in the polarization curves in Fig. 1(a and b). It can be seen that the corrosion potential is the same with or without Cl^-. The passive currents for ^2H_2O are lower than those obtained with H_2O, and in both cases, the respective currents are higher than that obtained without Cl^-. In the passive region, the anodic peak obtained at 0.15 V/SCE corresponds to the formation of titanium oxide identified by voltammetry in comparison with pure Ti. The critical pitting potential in transpassivity is not well defined and the passive region is the same indicating that pitting is unlikely to

TABLE VII Composition of deuterium oxide after corrosion of 316 Ti

Elements	Ni	Cr	Fe	Mo	Ti
(Wt μg %)	19.2	5.5	74.2	0.5	0.6

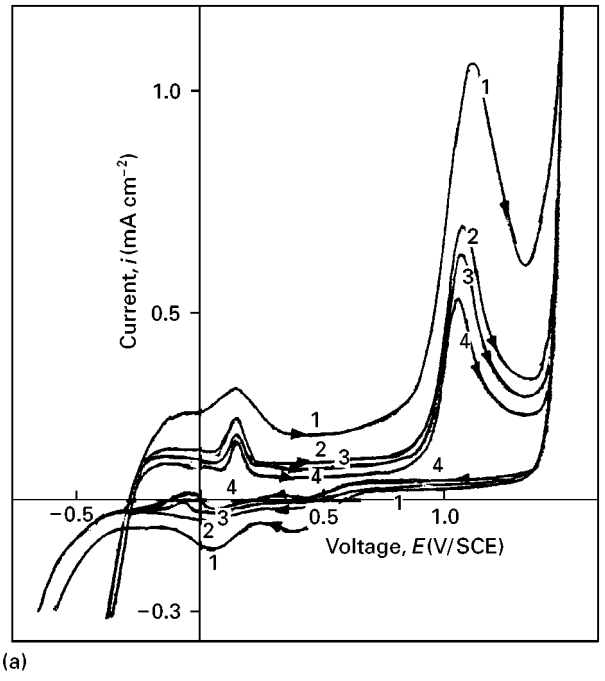

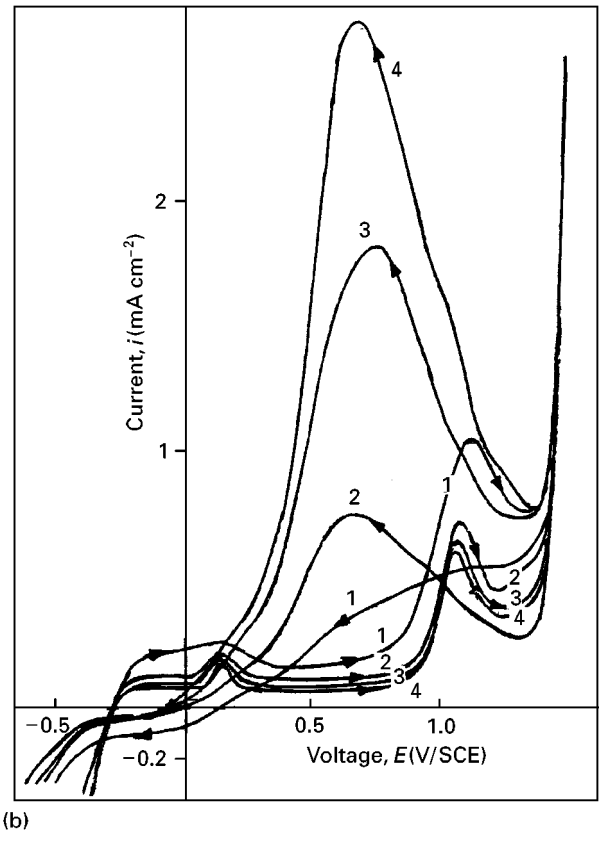

Figure 17 Voltammetric curves with Cl^- and ^2H_2O or H_2O at acid pH (A) 0.2 cm^2, ω: 2000 r.p.m., 0.05 mol dm^{-3} $NaNO_3$, scan rates: (**1**) 100. (**2**) 50, (**3**) 40 and (**4**) 30 mV s^{-1} (**a**) with H_2O , 0.02 mol dm^{-3} Cl^-, (**b**) with H_2O , 0.05 mol dm^{-3} Cl^-, (**c**) with ^2H_2O, 0.02 mol dm^{-3} Cl^- and (**d**) with ^2H_2O , 0.05 mol dm^{-3} Cl^-.

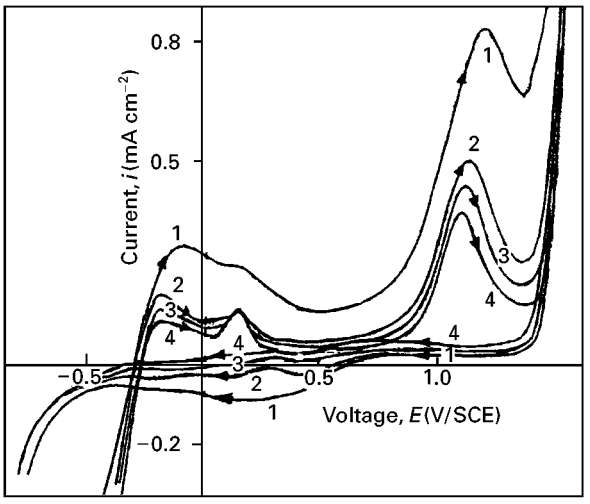

(c)

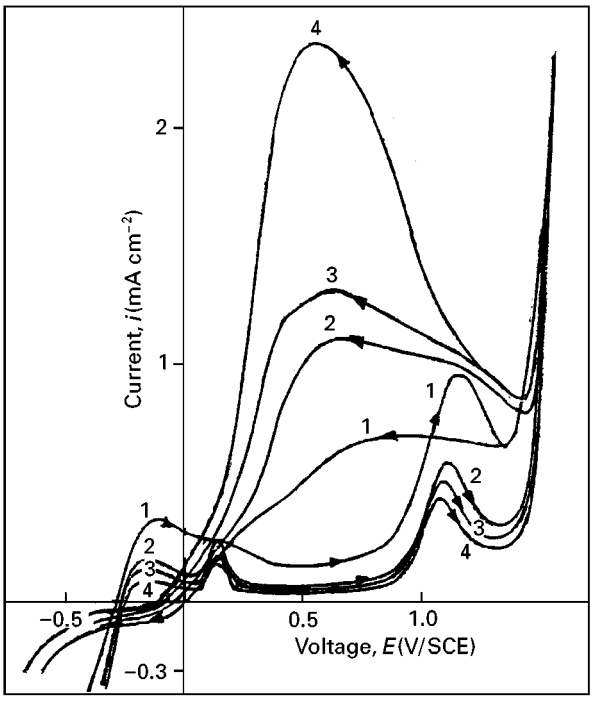

(d)

Figure 17 (Continued).

occur. At potentials above the pitting potential, pits are expected to grow. In the backward scans, it is seen that the anodic current increases with chloride concentration and is higher with ^2H_2O than H_2O, and returns to $\geq 200\,mV$ above the corrosion potential for ^2H_2O. According to the hysteresis shape, pits continue to initiate and grow after the scan reversal. These behaviours, decreasing intervals between E_{corr} and $E_{repassivation}$, suggest pitting followed by crevice corrosion with deuterium oxide.

The polarization curves obtained at more neutral pH are shown in Fig. 2(a and b). As shown above, the passive currents for ^2H_2O are lower than those obtained with H_2O, and in both cases, the respective currents are higher than that obtained without Cl^-. The corrosion potential shifts towards more positive values increasing the Cl^- concentration. With ^2H_2O, the passive potential domain decreases as the pitting potential shift towards lower values. As shown by the positive hysteresis shape in the backward scan, with ^2H_2O, the repassivity potential decreases more rapidly than that of H_2O when the Cl^- concentration increases, which makes it easy for crevice corrosion to occur. These different results imply that deuterium oxide does not provide better protection under these conditions, and the number of pits or the locally corroded area must increase. Metallographic examination (Fig. 15(a–c)) shows rod-shaped ferrite and cubic and pyramidal crystallites of titanium carbide coming from grain boundary decohesion. Magnetic measurements of ferrite give a concentration of 0.8%. In this case, as carbon is present (0.06%), chromium, molybdenum and titanium-rich carbides precipitate depleting the ferrite and grain boundaries in these elements. Localized corrosion and microcracks in the austenite/ferrite and titanium carbide borders of grain boundaries would arise. From scanning micrographs (Fig. 16(a–n)), it is seen for 1.5 V/SCE that the 316 Ti steel is highly corroded with localized corrosion: pitting, crevices and grain boundary decohesion leading to internal cavities expanding where the ferrite was present. The corrosion is also shown by the yellow colour of deuterium oxide and the purple-black precipitate (titanium hydroxide), whereas at 1 V/SCE no-pitting is seen by scanning electron microscopy. These two potentials correspond to, respectively, initiation and propagation of pits in the transpassive potentials (1.5 V/SCE), and without initiation (1 V/SCE), therefore pits cannot propagate or form. As titanium hydroxide precipitates at pH > 3, the ^2H_2O used was acidified to dissolve the metal cations before analyzing for Fe, Cr, Ni and Ti ions by atomic absorption spectrometry. The wavelengths were, respectively, 248.3, 357.9, 232.0 and 276.8 nm. The analysis results are given in Table VII. In comparison with Table II, these show essentially a weight loss for titanium, iron and nickel on the surface of 316 Ti steel. Along the grain boundaries there is localized corrosion of ferrite and formation of titanium carbide by the Cl^- and ^2H_2O.

The polarization curves obtained with chloride at alkaline pH are shown in Fig. 3(a and b). Two regions can be identified: the passive region and a sharply defined pitting region. The anodic current fluctuations obtained with deuterium oxide and the higher Cl^- concentration result from the occurrence of metastable pits (prepitting events) signifying breakdowns and repassivity alternatively in potentials close to pitting. 316 Ti steel remains passivated over a large potential domain. The transition potential (E_{pit}) decreases very slightly with a chloride concentration increase. As suggested by the shape of the positive and negative hysteresis, a few pits would continue to initiate and grow only in the beginning of the backward scan. This clearly defines a very small pitting potential region and shows that the passive oxide provides protection over a large potential domain. It can be seen that the corrosion potential increases with chloride, and the large deviation between E_{corr} and E_{pit} indicates no risk of crevice corrosion.

3.2.2. Voltammetric curves

In Fig. 17(a–d) realized at acid pH, a decrease in the scan rate leads to decreasing the passive and transpassive currents and the anodic peak of titanium oxide in the forward scan. In the backward scan, a decrease in the scan rate increases the pitting currents (Fig. 17b). It can also be seen that the repassive potential is higher at a high scan rate. At a low scan rate, chloride ions have the time to adsorb, then diffuse in the oxide layer by ionic vacancies leading to pitting following the kinetics. Using deuterium oxide, the repassivating potential is lower (Fig. 17d) than that of H_2O, signifying a greater possibility of crevice formation.

Fig. 18(a–d), realized at a more neutral pH, shows that the pitting current in the backward scan is higher than that obtained at acid pH and with ^2H_2O. In these figures, the anodic current increases with the scan rate and Cl^- concentration. By plotting the cathodic peak current as a function of scan rate, a straight line is obtained which fits the Levich equation:

$$i_p = 1.24F^{2/3}\Upsilon v^{0.5} A\omega^{0.5} C_{sp} \qquad (38)$$

where v is the scan rate, D the diffusion coefficient, A electrode surface, Υ the dynamic viscosity, F the Faraday constant and C_{sp} the species concentration. An experimental diffusion coefficient value of $5 \times 10^{-5}\,cm^2\,s^{-1}$ is then found and is close to the usual values found for aqueous media [43].

Tests realized at alkaline pH (Fig. 19) do not show any pitting current on varying scan rate. No current fluctuations are seen, the kinetics of oxide layer breakdowns are so slow that these scan rates they are not observable. There is no pitting propagation: pits are easily repassivated.

The explanation of the pitting behaviour obtained by polarization and voltammetric curves is helped as above by using the diagrams in Fig. 20 which show several characteristic changes depending on pH in the

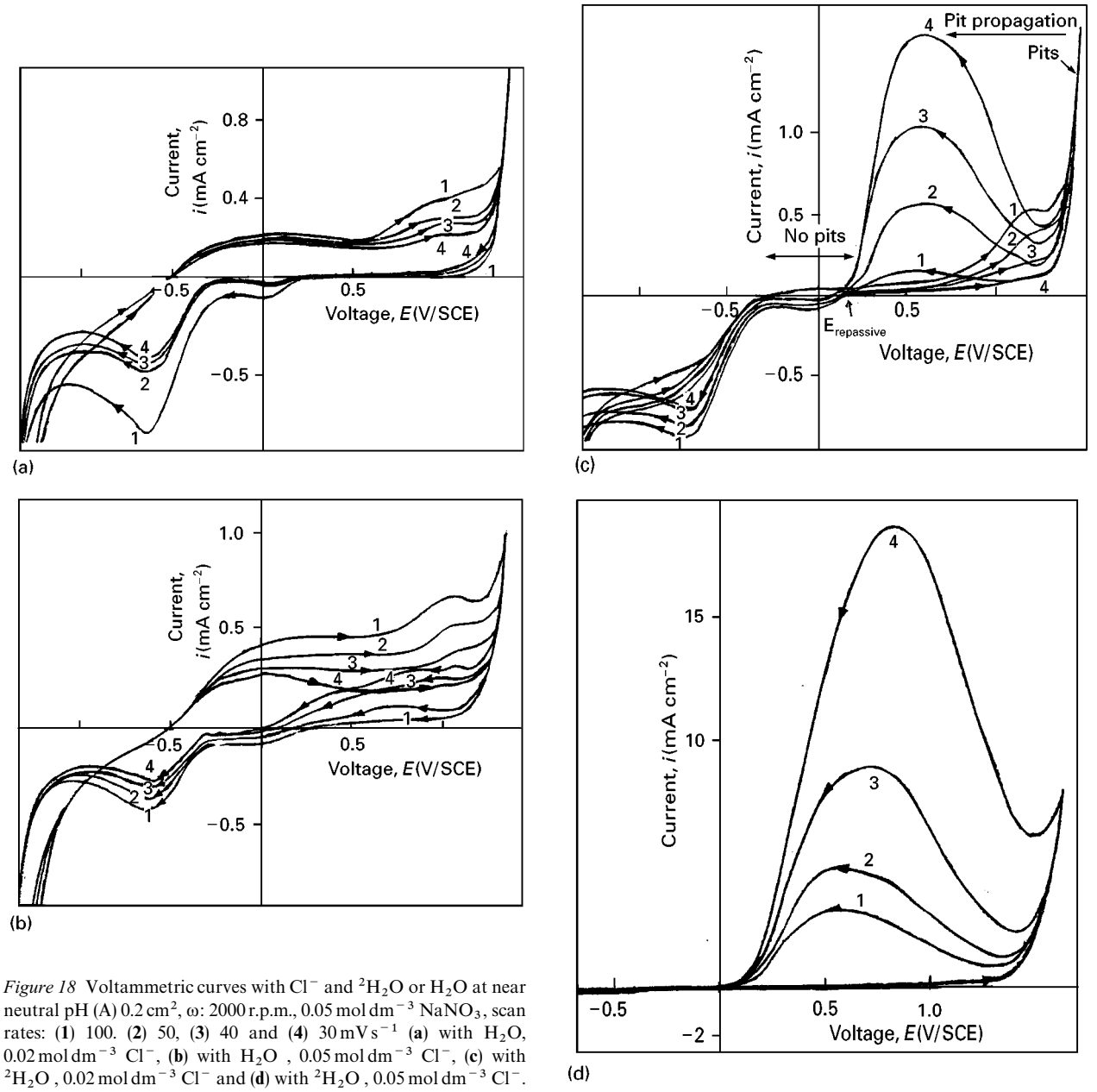

Figure 18 Voltammetric curves with Cl^- and ^2H_2O or H_2O at near neutral pH (A) 0.2 cm^2, ω: 2000 r.p.m., 0.05 mol dm^{-3} $NaNO_3$, scan rates: (**1**) 100. (**2**) 50, (**3**) 40 and (**4**) 30 mV s^{-1} (**a**) with H_2O, 0.02 mol dm^{-3} Cl^-, (**b**) with H_2O , 0.05 mol dm^{-3} Cl^-, (**c**) with ^2H_2O , 0.02 mol dm^{-3} Cl^- and (**d**) with ^2H_2O , 0.05 mol dm^{-3} Cl^-.

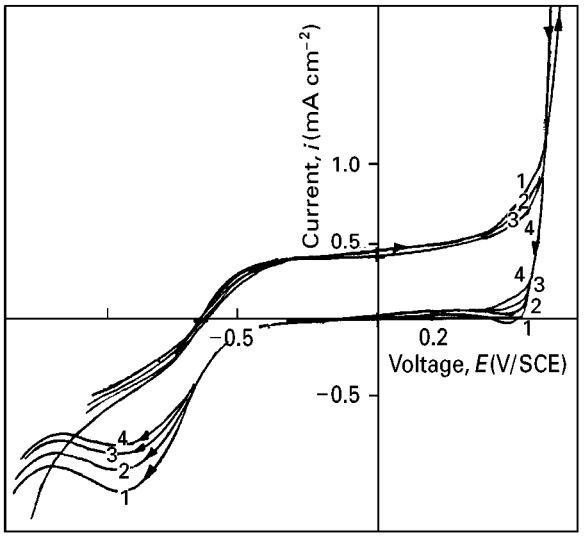

Figure 19 Voltammetric curves with Cl^- and ^2H_2O or H_2O at alkaline pH A: 0.2 cm^2, ω: 2000 r.p.m., 0.05 mol dm^{-3} $NaNO_3$, with 0.02 or 0.05 mol dm^{-3} Cl^-.

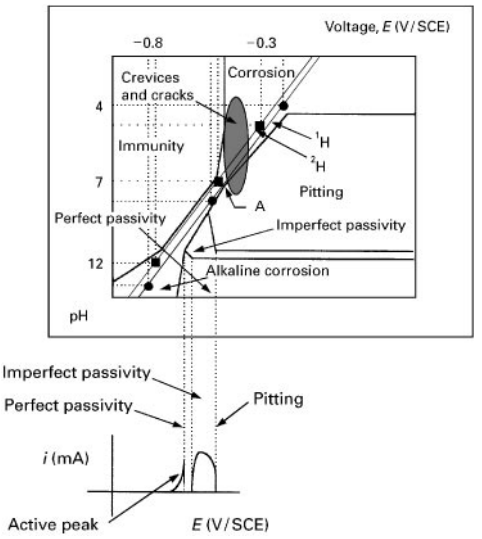

Figure 20 Diagram giving the behaviour of 316 Ti steel in water containing chloride (top), polarization curves in solution at pH 3–12 (bottom), experimental circumstances of general corrosion and perfect, non-perfect passivity, crevice corrosion and pitting [27].

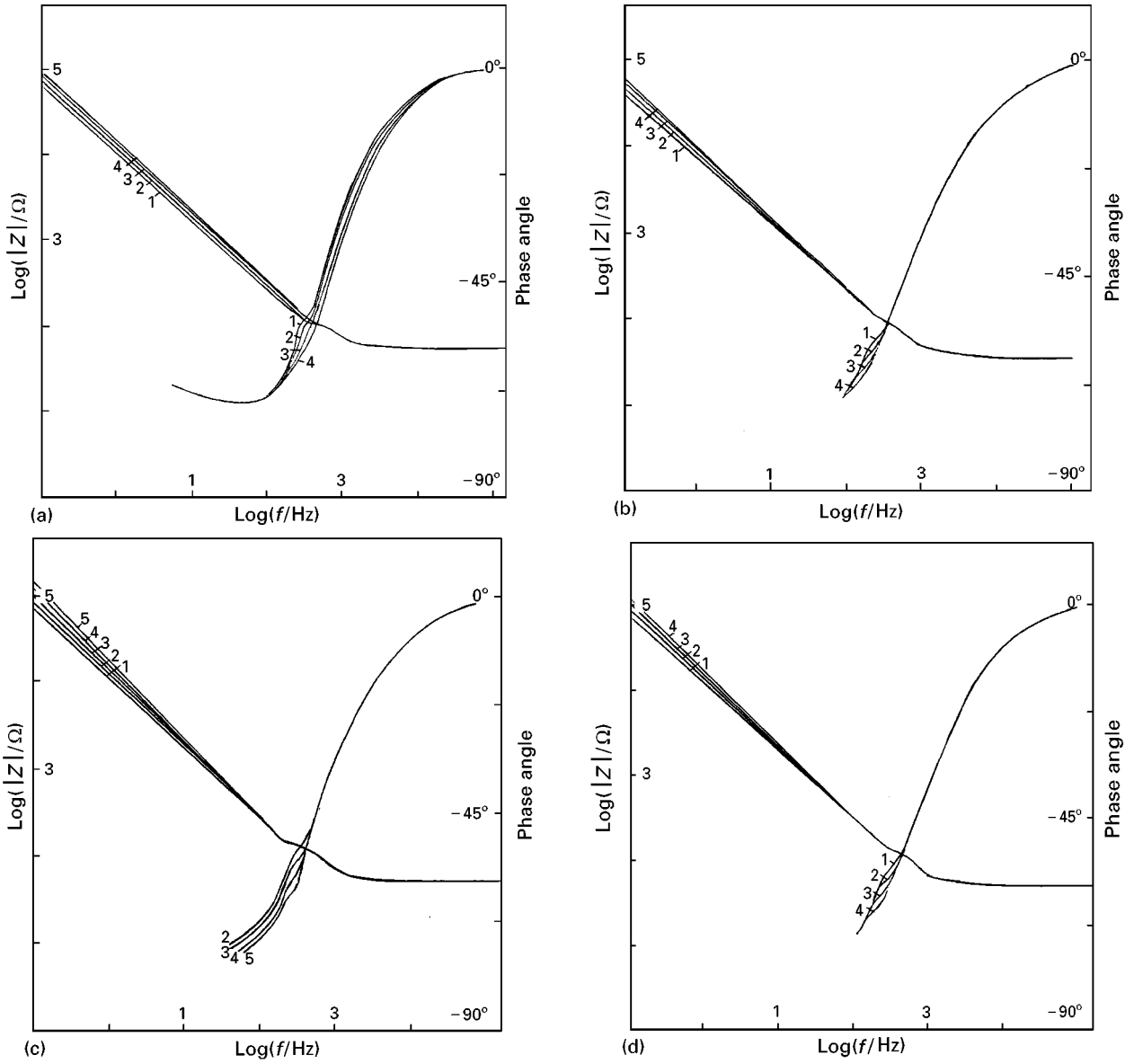

Figure 21 Experimental Bode spectra in passivity with ^2H_2O or H_2O at acid pH ω: 2000 r.p.m., A: 0.2 cm^2, 0.05 mol dm^{-3} $NaNO_3$ (**a**) with H_2O , 0.02 mol dm^{-3} Cl^-, (**1**) − 0.2. (**2**) − 0.17. (**3**) − 0.15 and (**4**) − 0.12 V/SCE (**b**) with H_2O, 0.05 mol dm^{-3} Cl^-, (**1**) − 0.2. (**2**) − 0.17. (**3**) − 0.15 and (**4**) − 0.12 V/SCE (**c**) with ^2H_2O, 0.02 mol dm^{-3} Cl^-, (**1**) − 0.2. (**2**) − 0.17. (**3**) − 0.15 (**4**) − 0.12 and (**5**) − 0.1 V/SCE (**d**) with ^2H_2O , 0.05 mol dm^{-3} Cl^-, (**1**) − 0.2. (**2**) − 0.17. (**3**) − 0.15 and (**4**) − 0.12 V/SCE, parameter values in Table VIII and IX.

Pourbaix relationship. At alkaline pH, perfect passivity for 316 Ti steel is seen. At more neutral pH, there is imperfect passivity and pitting with H_2O at pH 8, whereas with ^2H_2O, 316 Ti steel is more corroded by pitting and crevice corrosion at pH 7.5. At acid pH, the Cl^- concentration must be too low, and the polarization and voltammetric curves show a mixed behaviour: passivity and corrosion with greater possibility of pitting for ^2H_2O as seen in the experimental curves and in the Pourbaix relationship for pH 4.5 and 4.

3.2.3. Impedance diagrams

The experimental Bode plots obtained for 316 Ti steel at the corrosion potential and subjected to Cl^- in ^2H_2O and H_2O and drawn from about the corrosion potential are shown in Figs. 21(a–d), 22(a–d) and 23(a–d). The Bode plots are characterized as previously (section 3.1.3) by the same distinct regions. Data in Tables VIII and IX indicate that the oxide capacitance increased with Cl^-. The higher value ($48\,\mu F\,cm^{-2}$) obtained at pH 7.5 with ^2H_2O and $0.05\,mol\,dm^{-3}$ Cl^- would correspond to the double layer [43]. Comparison with Tables IV and V shows that the passive oxide layer is less insulating, signifying adsorption and diffusion of Cl^- within the passive oxide. This interpretation can be verified by determining the charge donor density (Fig. 24(a–c)). The values obtained are between $0.3–6 \times 10^{19}$ carrier cm^{-3} (Table X). These values, which are higher than those without Cl^-, indicate, from Equations 33–36, that the O^{2-} vacancies decrease and Me^{n+} vacancies in

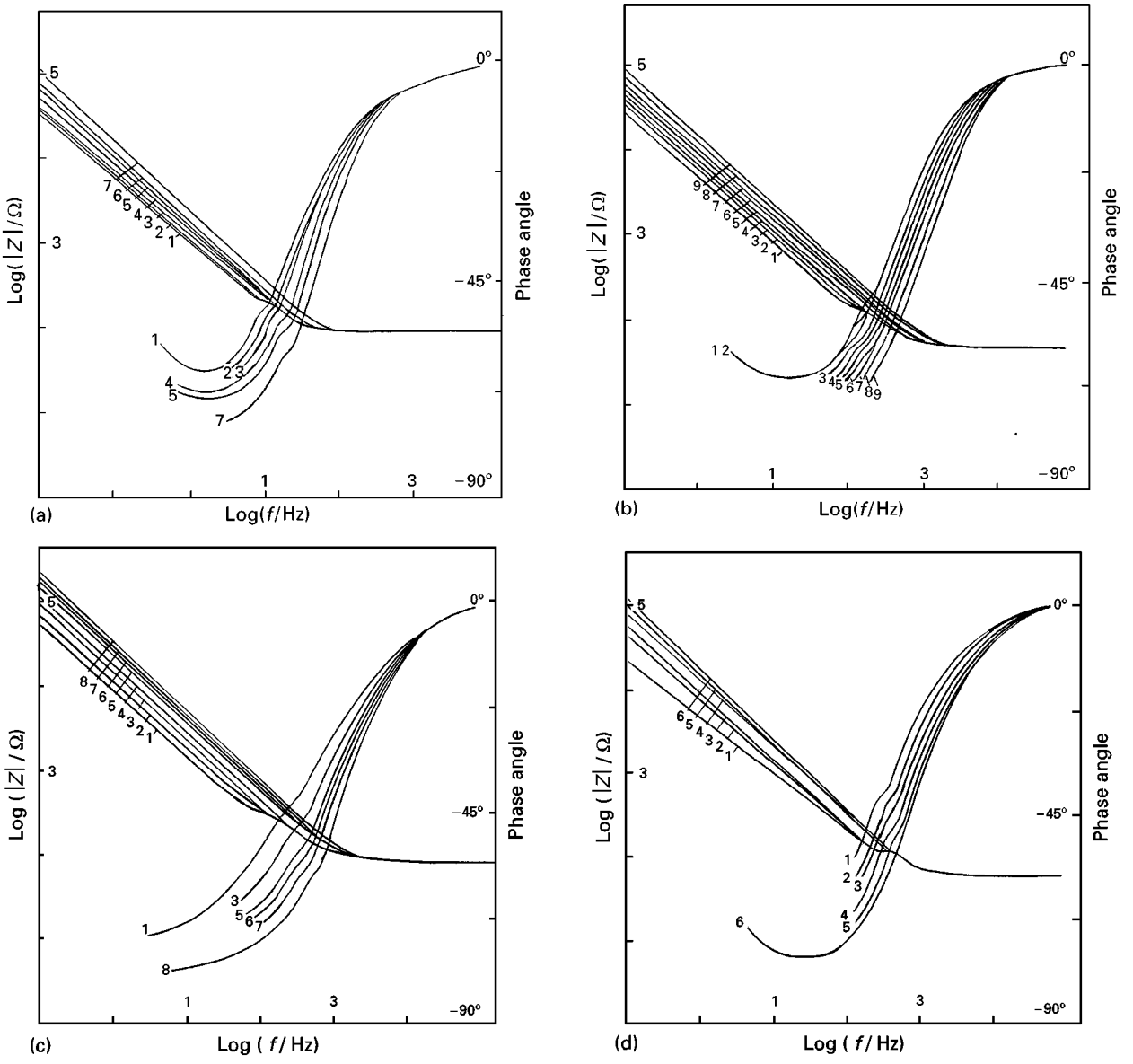

Figure 22 Experimental Bode spectra in passivity with ^2H_2O or H_2O at neutral pH ω: 2000 r.p.m., A: 0.2 cm^2, 0.05 mol dm^{-3} $NaNO_3$ (**a**) with H_2O , 0.02 mol dm^{-3} Cl^-, (**1**) − 0.3. (**2**) − 0.27. (**3**) − 0.25. (**4**) − 0.22. (**5**) − 0.2. (**6**) − 0.17 and (**7**) 0.15 V/SCE (**b**) with H_2O, 0.05 mol dm^{-3} Cl^-, (**1**) − 0.32. (**2**) − 0.3. (**3**) − 0.27. (**4**) − 0.25. (**5**) − 0.22. (**6**) − 0.2. (**7**) − 0.17. (**8**) − 0.15 V and (**9**) − 0.12 V/SCE (**c**) with ^2H_2O, 0.02 mol dm^{-3} Cl^-, (**1**) − 0.27. (**2**) − 0.25. (**3**) − 0.22. (**4**) − 0.2. (**5**) − 0.17. (**6**) − 0.15. (**7**) 0.12 and (**8**) − 0.1 V/SCE (**d**) with ^2H_2O, 0.05 mol dm^{-3} Cl^-, (**1**) − 0.27. (**2**) − 0.25. (**3**) − 0.22. (**4**) − 0.2. (**5**) − 0.17 and (**6**) − 0.15 V/SCE, parameter values in Tables VIII and IX.

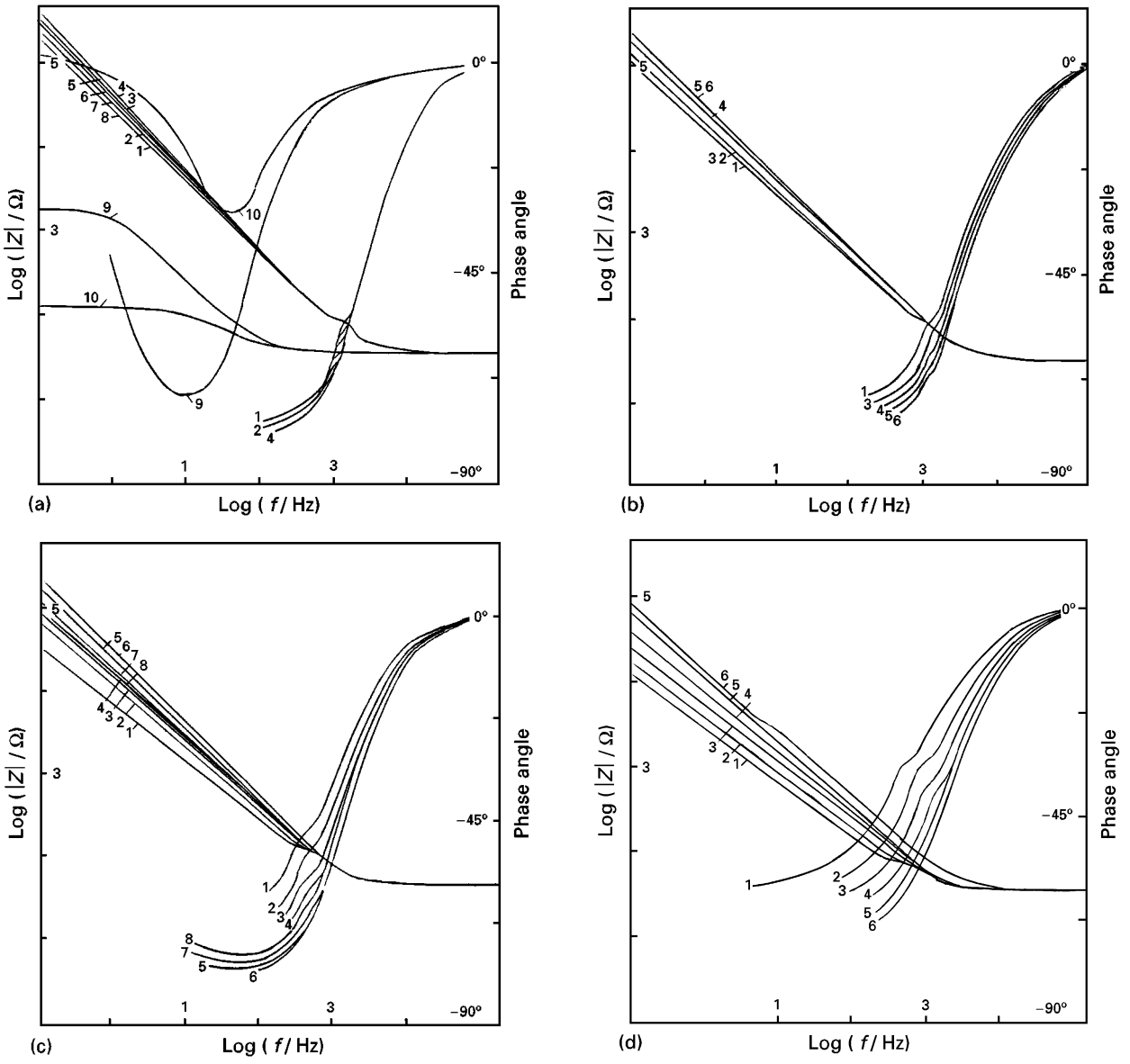

Figure 23 Experimental Bode spectra in passivity with ^2H_2O or H_2O at alkaline pH ω: 2000 r.p.m., A: 0.2 cm^2, 0.05 mol dm^{-3} $NaNO_3$ (**a**) with H_2O , 0.02 mol dm^{-3} Cl^-, (**1**) − 0.3 (**2**) − 0.27 (**3**) − 0.25 (**4**) − 0.22 (**5**) − 0.22 (**6**) − 0.17 (**7**) − 0.15 (**8**) − 0.12 (**9**) 0.6 and (**10**) 0.675 V/SCE (**b**) with H_2O, 0.05 mol dm^{-3} Cl^-, (**1**) − 0.35 (**2**) − 0.32 (**3**) − 0.3 (**4**) − 0.27 (**5**) − 0.25 and (**6**) − 0.22 V/SCE (**c**) with ^2H_2O, 0.02 mol dm^{-3} Cl^-, (**1**) − 0.45 (**2**) − 0.42 (**3**) − 0.4 (**4**) − 0.37 (**5**) − 0.35 (**6**) − 0.32 (**7**) − 0.3 and (**8**) − 0.27 V/SCE (**d**) with ^2H_2O, 0.05 mol dm^{-3} Cl^-, (**1**) − 0.45 (**2**) − 0.42 (**3**) − 0.4 (**4**) − 0.37 (**5**) − 0.35 and (**6**) − 0.32 V/SCE, parameter values in Tables VIII and IX.

TABLE VIII Dependence of oxide capacitance (μF cm^{-2}) on passive potentials with Cl^- and H_2O

	E (V/SCE)	− 0.35	− 0.32	− 0.3	− 0.27	− 0.25	− 0.22	− 0.2	− 0.17	− 0.15	−0.12
pH 4	0.02 mol dm^{-3} Cl^-							17	14	12	11
	0.05 mol dm^{-3} Cl^-							25	20	19	17
pH 8	0.02 mol dm^{-3} Cl^-			31	27	24	19	16	12	9	
	0.05 mol dm^{-3} Cl^-		42	32	29	25	21	18	14	11	8
pH 12.5	0.02 mol dm^{-3} Cl^-	8	6	5	4	3.7	3.5				
	0.05 mol dm^{-3} Cl^-	10	8	7	5	4.5					

TABLE IX Dependence of oxide capacitance (μF cm^{-2}) on passive potentials with Cl^- and ^2H_2O

	E (V/SCE)	−0.45	−0.42	−0.4	−0.37	−0.35	−0.32	−0.3	−0.27	−0.25	−0.22	−0.2	−0.17	−0.15	−0.12	−0.1
pH 4.5	0.02 mol dm^{-3} Cl^-											13	11	8	7	5
	0.05 mol dm^{-3} Cl^-											15	13	10	9	
pH 7.5	0.5 mol dm^{-3} Cl^-								23	17	14	10	9	7	6	4
	0.05 mol dm^{-3} Cl^-						48	30	25	19	16	13	11	9		
pH 12.5	0.02 mol dm^{-3} Cl^-	36	23	11	9	6	5	4	3.2							
	0.05 mol dm^{-3} Cl^-	40	25	14	11	7	6	5	4							

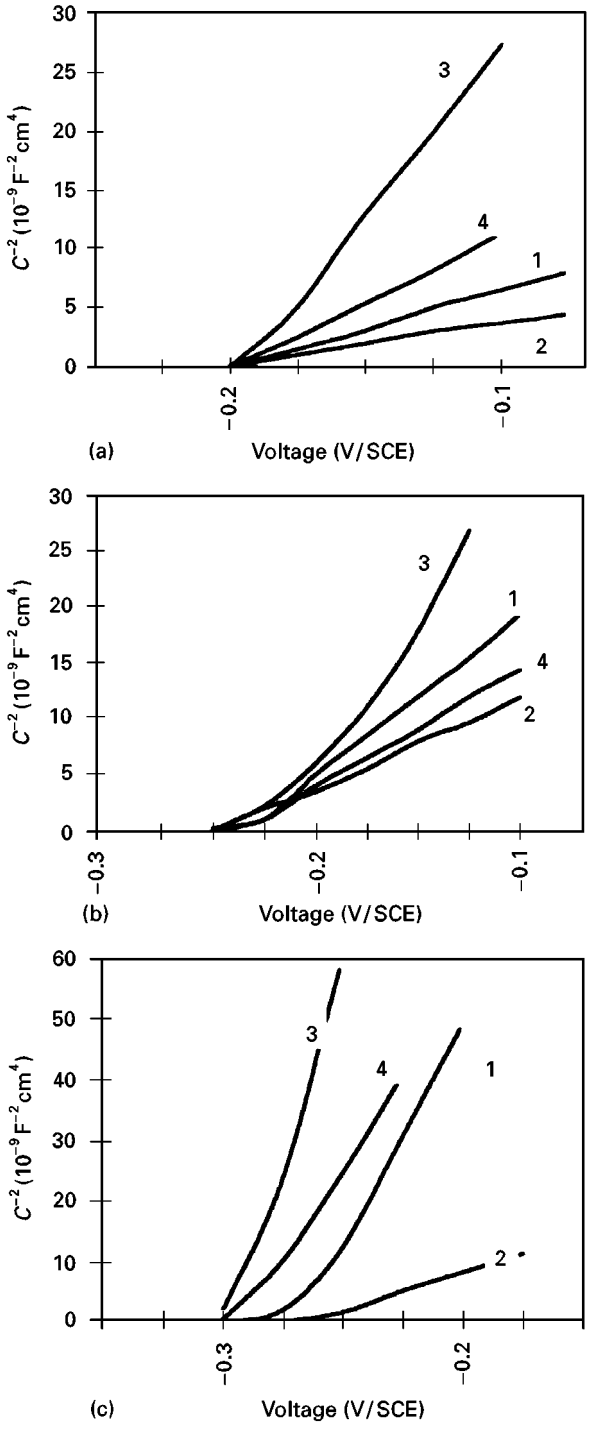

Figure 24 Mott–Schottky plots for passive oxide layer in ^2H_2O or H_2O and Cl^- media, (a) acid pH, (b) near neutral pH, (c) alkaline pH, curves 1 and 2: H_2O , curves 3 and 4: ^2H_2O with 0.02 and 0.05 mol dm^{-3} Cl^- respectively for each water.

equilibrium with metal cation increase with chloride, improving the diffusion. It thus appears that chloride ions adsorb and diffuse corresponding to the incubation period. Comparison between Figs. 13 and 24(a–c) shows that the flatband potential decreases with chloride which corresponds to the variation of oxide capacitance in agreement with Equation 30. The oxide thickness is also determined, its value is lower than without Cl^-. In the tables, for ^2H_2O, the oxide layer is more insulating in alkaline pH which corresponds to the perfect oxide in the Pourbaix relationship (Fig. 20).

The experimental Nyquist plots obtained for 316 Ti steel subjected to chloride in ^2H_2O are shown in Fig. 25. Along the capacitive semicircle, a linear unit slope region is observed. This is a characteristic of diffusion impedance. Changes in Cl^- concentration affect the frequency shift in the straight line and capacitive semicircle suggesting that the mass transport is dependent on the Cl^- concentration. The experimental

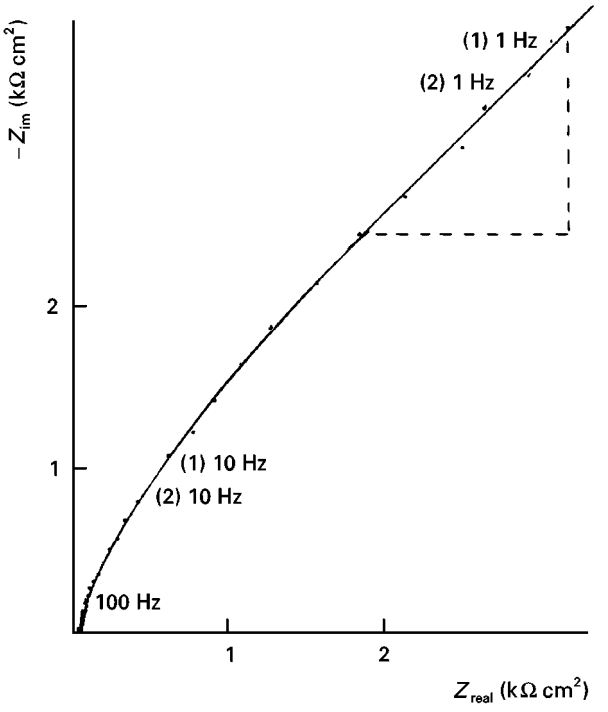

Figure 25 Nyquist plots with ^2H_2O and Cl^- pH 7.5, ω: 2000 r.p.m., *A*: 0.2 cm^2 0.05 mol dm^{-3}, $NaNO_3$, (**1**) 0.02 and (**2**) 0.05 mol dm^{-3} Cl^-, *E*: − 0.35 V/SCE.

TABLE X Thickness and donor density dependence on H_2O and ^2H_2O containing Cl^-

	Acid pH				pH near neutrality				Alkaline pH			
	H_2O		^2H_2O		H_2O		^2H_2O		H_2O		^2H_2O	
Cl^- (mol dm^{-3})	0.02	0.05	0.02	0.05	0.02	0.05	0.02	0.05	0.02	0.05	0.02	0.05
C_{ox}(μF cm^{-2})	11	17	5	9	9	8	4	9	3.5	4.5	3.2	4
d(nm)	1.1	0.7	1.7	1.3	1.8	1.1	2.5	1.3	2.7	1.1	4.8	2.7
$nd \times 10^{19}$	7	13	2	6	3	7	2	5	0.7	3	0.3	1

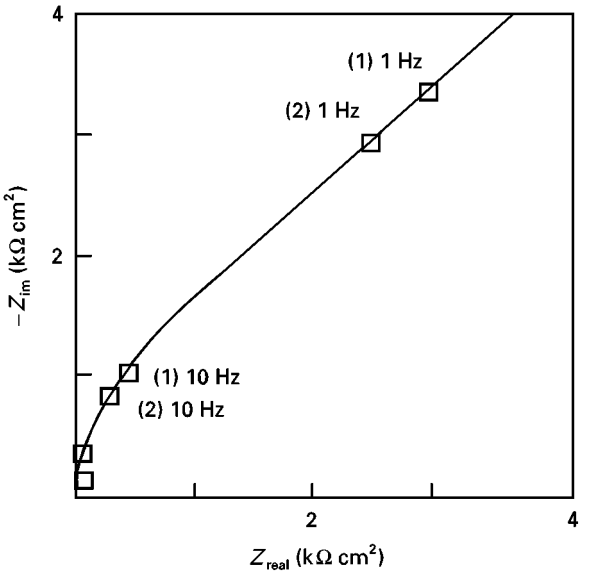

Figure 26 Simulated Nyquist plots with ^2H_2O and Cl^- parameter values in Table X.

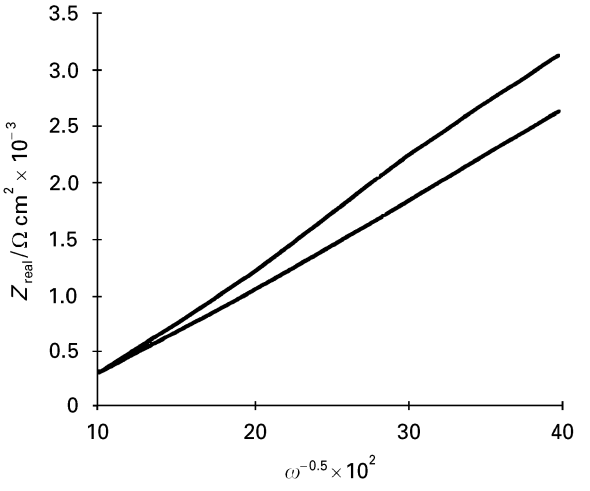

Figure 27 Electrode impedance as a function of angular frequency from Fig. 25.

diagrams can be satisfactorily explained on the basis of the equivalent circuit approach presented in Fig. 14c and the simulated spectra (Fig. 26) including a Randles diffusion impedance. The ionic diffusion coefficient (D) through the prepassive oxide layer can be determined uisng the spectra in the Warburg region. For this, Huggins *et al.* [44] have shown that Z_{real} as a fucntion of $\omega^{-0.5}$ varies linearly (Fig. 27) and its slop σ is equal to:

$$\sigma = \frac{RT}{n^2F^2A(2)^{1/2}}\left(\frac{1}{D^{0.5}C^{0.5}}\right) \qquad (39)$$

where σ is the Warburg coefficient, A the area and n the number of electrons transferred. The experimental slope of σ from Equation 39 is 8000 and 7000 $\Omega\,cm^2\,s^{-0.5}$ for 0.02 and 0.05 mol dm^{-3} Cl^-, respectively, which agree with the simulated value (Table XI). From these, the diffusion coefficients were calculated to be 0.9 and 1.5×10^{-18} $cm^2\,s^{-1}$. The ionic diffusion coefficient increases slightly with Cl^- concentration and appears much lower inside the passive oxide layer than in deuterium oxide (Equation 38). These values indicate that the prepassive oxide layer is present at the corrosion potential (see section 3.1.1. on the effect of intermediate deuterated metal oxide).

TABLE XI Dependence of Warburg impedance on ^2H_2O and Cl^- at -0.3 V/SCE and pH 7.5

Cl^- (mol dm^{-3})	0.02	0.05
W ($\Omega\,cm^2\,s^{-0.5}$)	8000	7000

4. Conclusions

Without chloride, it is experimentally shown that deuterium oxide modifies the corrosion potential due to the positive or negative displacement in pH between ^2H_2O and H_2O as indicated in the potential–pH relationship. This modification of pH also contributes to changing the size of active and transpassive peaks and the passive current value. At the different pH values studied and with ^2H_2O, 316 Ti steel is less corroded in the active region and corrosion potential. The oxide layer capacitance, thickness, donor density and flatband potential were determined at different passive potentials for ^2H_2O and H_2O. The capacitance and donor density are lower with deuterium oxide. These values indicate the formation of a more perfect passive oxide and better protection with ^2H_2O.

With Cl^- and acid pH or near neutral pH and with ^2H_2O, the critical pitting potential is in transpassivity indicating that pitting is unlikely to occur for 316 Ti steel. The repassive potential is around $+200$ mV above the corrosion potential, therefore crevice corosion is expected. Scanning electron microscopy and optical examinations show effectively that 316 Ti steel is locally corroded at high potentials by pitting and grain boundary dissolution leading to crevice corrosion and internal cavities. Localized corrosion produces titanium carbide crystallites and ferrite/ austenite borders along grain boundaries. These different results imply that deuterium oxide does not provide better protection with chloride for the transpassivity. The results obtained in the passive potentials at the beginning of passivity show that the passive oxide layer is more insulating with ^2H_2O than H_2O, but the oxide capacitance and donor density are higher than without chloride. These values indicate the formation of a less perfect passive oxide. At alkaline pH, perfect passivity is obtained as shown in the potential–pH relationship and experimental results.

References

1. G. BELLANGER and J. J. RAMEAU, *Corros. Sci.* **36** (1994) 545.
2. G. BELLANGER, *J. Nucl. Mater.* **210** (1994) 63.
3. *Idem*, *J. Mater. Sci.* **30** (1995) 1259.
4. *Idem*, *J. Nucl. Mater.* **217** (1993) 187.
5. G. BELLANGER and J. J. RAMEAU, *J. ibid.* **226** (1995) 104.
6. *Idem.*, *Electrochim. Acta* **15** (1995) 2519.
7. A. ROUSTILA, N. KUROMOTO, A. M. BRASS and J. CHÊNE, *J. Nucl. Mater.* **211** (1994) 156.

8. A. M. BRASS, J. CHÊNE and J. GONZALEZ, *Metall. and Mat. Trans.* **25A** (1994) 1159.
9. G. BELLANGER and J. J. RAMEAU, *Fusion Technol., J. Am. Nucl. Soc.* **24** (1993) 145.
10. G. BELLANGER, *Ibid* **27** (1995) 46.
11. E. BEDNARKIEWICZ and Z. KUBLIK, *Electrochim. Acta* **24** (1979) 121.
12. A. BRUGGEMAN, M. SNYKERS and P. DE REGGE, *Fusion Technol. J. Amer. Nucl. Soc.* **14** (1988) 828.
13. W. G. BURNS and P. B. MOORE, *Radiation Effects* **30** (1976) 233.
14. J. K. LINACRE and W. R. MARSH, report R 10027, Chemistry Division, Atomic Energy Research Establishment, Harwell (1981).
15. J. WRIGHT, J. K. LINACRE, W. R. MARSH and T. H. BATES, in Proc. Int. Conf. on the Peaceful Uses of Atomic Energy, Vol. 7, Geneva, 1955 (United Nations, New York, 1956) p. 560.
16. J. P. DIARD, P. LANDAUD, B. LE GORREC and C. MONTELLA, in Proceedings Deuxième Forum sur les Impédances Electrochemiques, Montrouge, France, 1987 (University P. & M. Curie, Paris, 1987).
17. J. P. DIARD, B. LE GORREC, S. MAXIMOVITCH, *Electrochim. Acta* **35** (1990) 1099.
18. V. A. MACAGNO and J. W. SCHULTZE, *J. Electroanal. Chem.* **180** (1984) 157.
19. J. W. SCHULTZE and V. A. MACAGNO, *Electrochim. Acta* **31** (1986) 355.
20. L. YOUNG, "Anodic oxide films", (Academic Press, London, 1961).
21. O. KERREC, D. DEVILLIERS, C. HINNEN and P. MARCUS, in Symp. Modifications of Passive Films (European Federation of Corrosion, London, 1994) p. 206.
22. O. KERREC, PhD thesis, Paris, (1992).
23. W. WILHELMSEN, *Electrochim. Acta* **33** (1988) 63.
24. G. BELLANGER and J. J. RAMEAU, *J. Nucl. Mater* **31** (1996) 2097.
25. S. ZECEVIC, D. M. DRAZIC and S. GOJKOVIC, *Electrochim. Acta* **36** (1991) 5.
26. P. E. MORRIS and R. C. SCARBERRY, *Corrosion* **26** (1970) 169.
27. J. VAN MUYLDER, in "Comprehensive treatise of electrochemistry", Vol. 4, edited by J. O'M. Bockris, B. E. Conway, E. Yeager and R. E. White (Plenum Press, New York, 1981) pp. 1–96.
28. CHONG-CHENG HUANG, WEN-TA TSAI and JU-TUNG LEE, *Mater. Sci. Engng.* **A190** (1995) 199.
29. J. M. ALBELLA, I. M. MONTERO and J. I. MARTINZ-DUART, *Thin Solid Film* **125** (1985) 57.
30. M. W. BREITER, *Electrochim. Acta* **15** (1970) 1145.
31. O. KERREC, D. DEVILLIERS, H. GROULT and M. CHELMA, *ibid* **40** (1995) 719.
32. P. SCHMUKI and H. BÖHNI, *ibid* **40** (1995) 775.
33. E. B. CASTRO and J. R. VILCHE, *ibid* **38** (1993) 1567.
34. A. M. P. SIMOES, M. G. S. FERREIRA, B. RONDOT and M. DA CUNHA BELO, *J. Electrochem. Soc.* **137** (1990) 1.
35. RAK-HYUN, SU-IL PYUN and R. A. ORIANI, *J. Appl. Electrochem.* **21** (1991) 181.
36. J. R. MACDONALD, "Impedance spectroscopy", (Wiley, New York, 1987).
37. K. JÜTTNER, *Electrochim. Acta* **35** (1990) 1501.
38. T. PAJKOSSY and L. NYIKOS, *Acta Chim. Hung.* **117** (1984) 417.
39. C. Y. CHAO, L. F. LIN and D.D. MACDONALD, *J. Electrochem. Soc.* **128** (1981) 1187.
40. J. B. BESSONE, D. R. SALINAS, C. E. MAYER, M. EBERT and W. J. LORENZ, *Electrochim. Acta* **37** (1992) 2283.
41. H. H. STREHBLOW, in "Corrosion mechanisms in theory and practice", edited by P. Marcus and J. Oudar (Dekker, New York, 1995) p. 201.
42. C. Y. CHAO, L. F. LIN and D. D. MACDONALD, *J. Electrochem. Soc.* **128** (1981) 1194.
43. A. J. BARD and L. R. FAULKER, "Electrochemical methods. Fundamentals and applications", (Wiley, New York, 1980).
44. R. A. HUGGINS, I. D. RAISTRICK and C. K. HO, *J. Electrochem. Soc.* **127** (1980) 343.

Received 25 March 1996
and accepted 28 January 1997